

*Chapter VII***Other Mothers: Effects of Additives to the Mother Phase on Bubble Nucleation**

“With a Little Help from My  
Friends”

---

by John Lennon / Paul McCartney

*High-pressure sampling experiments were performed at the Dow TXINN research facility in Lake Jackson, TX, with the tremendous help of Dr. Thomas C. Fitzgibbons, Marla Gilbert, and Dr. James Griffith. The experiment was designed by Dr. Bill Winniford, Dr. Steve Horvath, Dr. James Griffith, Dr. Thomas C. Fitzgibbons, and Prof. Julie Kornfeld. Dr. Brenton L. Drake provided invaluable assistance with safety precautions to mitigate the risk of flammability when using cyclopentane. The discovery of the prediction of two-stage bubble nucleation with the string method, as well as the development of the PC-SAFT model of ternary phase behavior are the work of Dr. Huikuan Chao under Prof. Zhen-Gang Wang.*

In Chapter I, we proposed to study a model system of polyurethane consisting of polyol and CO<sub>2</sub> instead of a complete polyurethane formulation. By studying a simple system, we could focus on a single driving force for the nucleation of bubbles—the supersaturation of dissolved CO<sub>2</sub>—which simplified instrument development (Chapter III) and analysis of nucleation (Chapter VI). However, bubble nucleation in polyurethane is affected by the many other components involved, such as chemically reactive isocyanate, hydrocarbon-based physical blowing agents (PBAs), water (chemical blowing agent), surfactants, catalysts, and flame retardant, and the processing conditions, such as temperature increase and cross-linking reaction. While a high-quality polyurethane foam typically requires each of these aspects to work in concert, studying the effect of adding each one-by-one on bubble nucleation can elucidate the specific role of each in a way that previous work on complete formulations cannot.

In this Chapter, we present our first steps toward understanding the individual effects of these other aspects of polyurethane foaming, focusing primarily on the effect of adding cyclopentane, a hydrocarbon physical blowing agent (PBA) used to

replace ozone-depleting PBAs like CFCs and HCFCs (Section I.3). We focused on cyclopentane because its role in polyurethane foaming and, more specifically, in bubble nucleation during polyurethane foaming is not well understood. As discussed in Section I.3, the primary motivation to add cyclopentane in commercial polyurethane foam formulations is that the heat released by the exothermic polyurethane and urea synthesis reactions vaporizes the initially liquid cyclopentane early in the foaming process (the boiling point of cyclopentane is 49 °C, while the PU foam can reach 120 °C [1] to 190 °C [2]). Many studies have shown that the addition of cyclopentane increases bubble nucleation and decreases cell size in polyurethane foaming [3–5]. In all of these experiments, however, the polyurethane foam is heated above the boiling point of cyclopentane (49 °C), so the increase in bubble nucleation is explained as the result of vaporizing cyclopentane enough to nucleate on its own, independent of the CO<sub>2</sub> or other blowing agents involved.

Here, we will explore the role that cyclopentane plays in enhancing nucleation of CO<sub>2</sub>-rich bubbles. This question has not been considered in the literature to our knowledge, but is motivated by findings in related systems. In a ternary mixture of polymer, solvent, and gas (like polyol, cyclopentane, and CO<sub>2</sub>), a three-phase coexistence is both predicted [6] and observed [7] to be thermodynamically stable within a finite window of temperature and pressure. The significance of three-phase coexistence for nucleation behavior was highlighted by Müller *et al.* [8], who showed that, near a three-phase region, a solvent-rich liquid wets the interface of bubble embryos and may condense into a liquid-like phase in the bubble interior. This partial condensation reduces the interfacial tension along the bubble relative to a vapor-like bubble, which reduces the nucleation energy barrier, as first predicted in a binary mixture of polymer and gas by Talanquer and Oxtoby [9]. Bubble nucleation may proceed through this partially condensed state even if it is not thermodynamically favorable as a result of Ostwald's rule, which states that the nucleated phase may be that which is closer in free energy to the mother phase rather than the phase with the minimum free energy [10]. Such a low-barrier pathway to nucleation would not require the addition of heat. We show experimentally that the addition of cyclopentane significantly increases the bubble nucleation rate without the addition of heat in the vicinity of an experimentally demonstrated three-phase coexistence. We also present a theoretical model using string method based on DFT to show that the addition of cyclopentane opens up a two-stage nucleation pathway with a significantly lower nucleation barrier, something that classical nucleation theory cannot capture.

We also briefly discuss the effect of adding surfactant. Surfactants are added to polyurethane foams both to reduce the energy barrier to nucleate bubbles (by reducing the interfacial tension that opposes nucleation) and to stabilize bubbles as they grow [2].

Many other studies have explored the effects of adding solid particles to increase bubble nucleation. As discussed in Section I.3, solid particles are not typically included in rigid polyurethane foam (RPUF) formulations [11]. Given their limited use in industry and the challenges of thoroughly cleaning out nanoparticles between experiments, we did not explore their effects on bubble nucleation in the present work. Nevertheless, the addition of particles can provide unique insight into the role of particles in the current system, as discussed in Section VII.4.

Polyurethane foams also contain flame retardants and chemical catalysts that drive the polyurethane synthesis reaction. Their effects on bubble nucleation have not been thoroughly explored in the literature. These compounds are added in small quantities and are not intended to change the foam structure, but a study to verify the assumption that they have a negligible effect on bubble nucleation would be valuable.

## **VII.1 Adding Cyclopentane Dramatically Increases Bubble Nucleation in Polyol–CO<sub>2</sub> Foam**

### **Estimating Nucleation Rate from Bubble Counts**

We demonstrate that adding cyclopentane increases bubble nucleation by estimating bubble nucleation rates from a foaming experiment performed under identical conditions as that in Section VI.4. In this case, however, cyclopentane was mixed with the polyol (PPG 2700 g/mol) in a ratio of 1:5 by weight before dissolving CO<sub>2</sub> into the solution inside a Parr reactor. Based on the PC-SAFT model of this ternary mixture of PPG 2700 g/mol, cyclopentane, and CO<sub>2</sub> described in Section VII.3, under the saturation pressure of 7.2 MPa near laboratory temperature of 22 °C, the resulting mixture would be roughly 50% PPG, 10% cyclopentane, and 40% CO<sub>2</sub> by weight. Because few of the measurements of bubble nucleation in the PPG–CO<sub>2</sub> mixtures shown in Chapter VI contained enough data points to estimate the nucleation rate by the exponential decay in the incubation time (see Figure VI.1), we first estimate the nucleation rate in the PPG–cyclopentane–CO<sub>2</sub> mixture using the method of converting counts of nucleation events at a given supersaturation into a nucleation rate (as depicted in Figure VI.2). These estimates of the nucleation rate

for the mixtures with and without cyclopentane are shown in Figure VII.1.

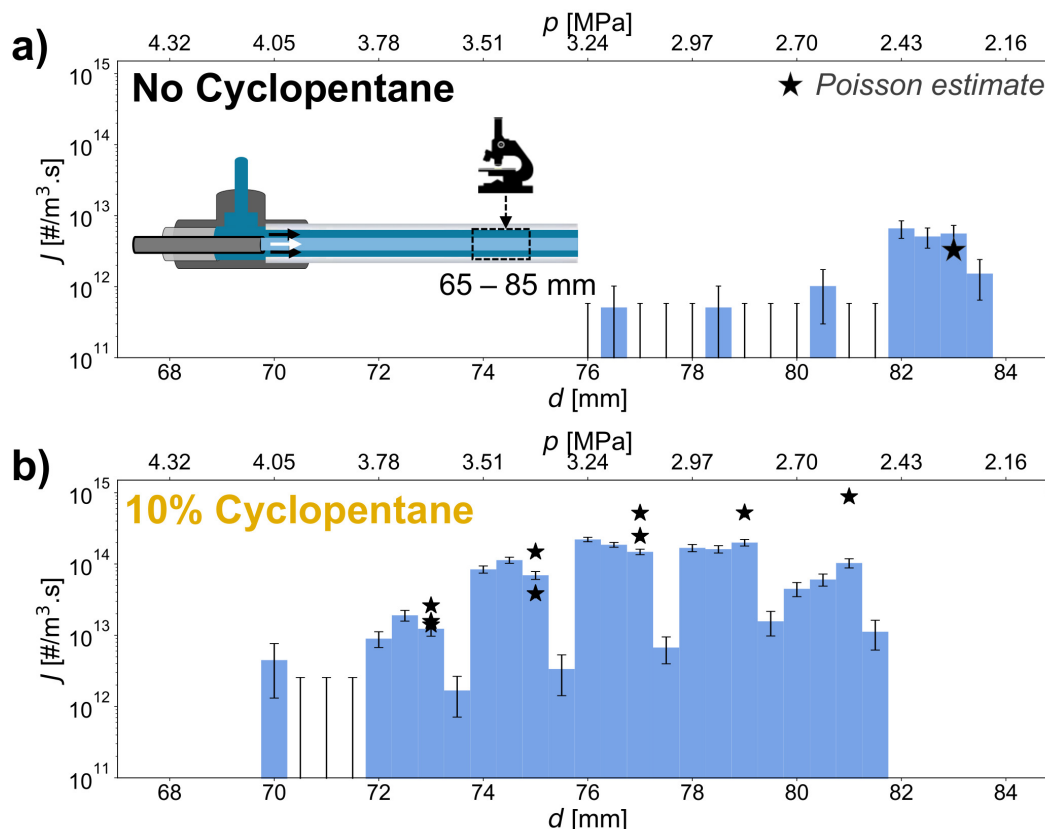


Figure VII.1: Comparison of bubble nucleation rate  $J$  vs. supersaturation estimated by counting nucleation events at different locations along the observation capillary  $d$  (lower horizontal axis), which corresponds to different fluid pressures  $p$  (upper horizontal axis). In both cases, the polyol is PPG 2700 g/mol,  $\text{CO}_2$  is saturated at 7.2 MPa and 22 °C, and the inlet pressure was 13.1td a) Mixture of polyol and  $\text{CO}_2$  (same as in Figure VI.2b). b) Mixture of polyol, cyclopentane, and  $\text{CO}_2$  prepared under the same conditions, for which polyol and cyclopentane were added in a ratio of 5:1 by weight. Stars indicate the estimates of the nucleation rate by fitting the inter-nucleation times to an exponential decay based on Poisson statistics described in Section VI.1; error bars are shown but are smaller than the markers.

Bubble nucleation in the mixture containing cyclopentane (C5) (Figure VII.1b) occurs at a lower degree of supersaturation (higher pressure) and at a faster rate than in the mixture without cyclopentane (Figure VII.1a). While the mixture without cyclopentane does not exceed an estimated bubble nucleation rate of  $10^{13}/\text{m}^3 \cdot \text{s}$  until the pressure is estimated below 2.4 MPa, the mixture with cyclopentane does so at an estimated pressure of 3.5 MPa. Once the pressure has dropped to 2.4 MPa, the nucleation rate in the mixture containing cyclopentane has increased by at least an order of magnitude. Because the current algorithm does not

exclude the volume occupied by elongated bubbles (see discussion in Section VI.5), which become more frequent at lower pressures, the true nucleation rate is likely higher. Interestingly, the bubble nucleation rate for the mixture with cyclopentane does not increase as abruptly as the measurements of the rate for the mixture without cyclopentane appeared to suggest. Rather, the bubble nucleation rate increases quickly but steadily, similarly to the prediction by the string method shown in Figure VI.6b. Last, it is possible that the increased number of bubbles in the inner stream in the mixture with cyclopentane results in a lower fluid pressure near the outlet of the observation capillary than in the mixture without cyclopentane, where there were fewer bubbles. Consequently, the estimated pressures may be lower for the mixture with cyclopentane than listed. Nevertheless, even if the pressure were overestimated for the mixture containing cyclopentane, the cause of the overestimation would be the increased amount of bubble nucleation relative to the mixture not containing cyclopentane. Therefore, we can still conclude that the addition of cyclopentane significantly increased bubble nucleation and reduced the supersaturation required to nucleate bubbles.

### **Estimating Nucleation Rate from Poisson Statistics**

Because of the high rate of bubble nucleation in the mixture containing cyclopentane, enough bubbles could be detected in experiments to estimate the nucleation rate from the exponential decay of the incubation time (as depicted in Figure VI.1). Not only was the rate higher, but visual observation showed that small, spherical bubbles were less likely to be interrupted by elongated bubbles, leading to a higher proportion of consecutive bubble nucleation events. In fact, the number of consecutive observations of bubble nucleation was so much higher with cyclopentane that we could test for the exponential decay of the incubation time characteristic of a Poisson process much more rigorously than in Chapter VI. One example of the exponential fit to this decay is shown in Figure VII.2. Whereas fewer than ten nucleation events were available for the analysis of bubble nucleation in the PPG–CO<sub>2</sub> mixture in Figure VI.1, almost 300 were available for the analysis of bubble nucleation in the PPG–cyclopentane–CO<sub>2</sub> mixture in Figure VII.2. The distribution of the incubation times of these events is shown in panel (a) and the decay of the number of non-nucleated “samples”  $N$  (see discussion of this method in Section VI.1) is shown in panel (b). The exponential fit (dashed line) fits the data well, providing stronger support of our hypothesis that the bubbles we are observing nucleate according to a Poisson process, and thus behave as if they were nucleated

by homogeneous nucleation.

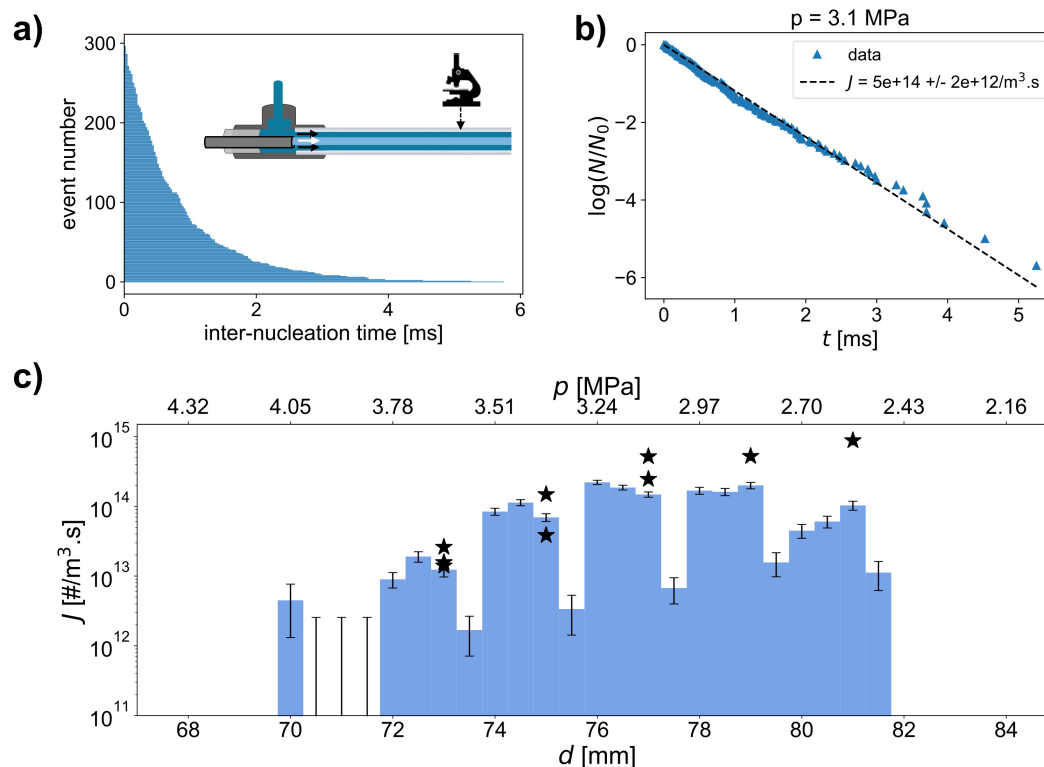


Figure VII.2: Exponential decay method for estimating nucleation rate of PPG–C5–CO<sub>2</sub> mixture under the same experimental conditions as in Figure VII.1. a) Inter-nucleation times as measured at 77 mm along the observation capillary (fluid pressure of  $p = 3.1$  MPa, depicted schematically on diagram of microfluidic channel) according to the technique described in Section VI.1 for each nucleation event detected. b) The logarithm of the fraction of non-nucleated fluid samples  $\log(N/N_0)$  (blue triangles) plotted as a function of time and fit to an exponential function (dashed line). A lower bound on the nucleation rate  $J$  is estimated by dividing the frequency (the decay constant of the exponential fit) by the volume of fluid (some of which is depleted of CO<sub>2</sub>). c) Nucleation rate  $J$  as a function of distance along the observation capillary  $d$  (lower horizontal axis) and estimated pressure in the capillary  $p$  (upper horizontal axis). The bars represent the nucleation rate estimated by counting nucleation events in each segment of the capillary (same a Figure VII.1b). The bars decrease every 2 mm due to diminished detection of bubbles along the edges of the field of view caused by vignetting—we expect these rates to be similar to those nearby. The nucleation rate estimated from fits such as the one shown in (b) are superimposed (black stars). The nucleation rate was lower when the same measurements were performed a few hours later—these are omitted since we do not know how the system may have changed during this time.

As discussed in Section VI.1, the decay constant of the exponential fit to the decay of non-nucleated samples  $N$  gives the frequency of bubble nucleation,

which can be converted into the nucleation rate  $J$  by dividing by the observed volume. In Figure VII.2c, the nucleation rate estimated in this way is superimposed as stars on the bar chart of nucleation rate estimated by counting nucleation events (same bar chart as in Figure VII.1b). Note that the nucleation rate estimated with Poisson statistics upon the addition of cyclopentane is similar in Figure VII.2 as in Figure VI.1d without cyclopentane, yet the number of consecutive nucleation events was much higher for cyclopentane (compare with Figure VI.1b). This discrepancy is likely the result of having fewer interruptions of consecutive nucleation events by elongated bubbles, which become more common farther downstream, as was the case for the measurement in Figure VI.1b,d. Both methods of estimating the nucleation rate are within an order of magnitude of each other and show a similar rate of increase in the nucleation rate with decreasing pressure. We still expect that the volume of fluid by which we divide the frequency to obtain the nucleation rate  $J$  is overestimated, and thus, the nucleation rate is underestimated (see discussion in Section VI.5), but the rough agreement between the two methods suggests that the estimates of nucleation rate are consistent. This consistency further supports our conclusion that the addition of cyclopentane significantly increases the rate of bubble nucleation and allows for bubble nucleation at a lower supersaturation. In the next Section, we explore a possible explanation for this effect by adapting our string method model from Section VI.3 to a ternary mixture of PPG, cyclopentane, and CO<sub>2</sub>.

## VII.2 String Method Based on DFT Predicts Two-stage Bubble Nucleation with Cyclopentane

Using the string method based on DFT described in Section VI.3, we estimated the nucleation pathway of supersaturated mixtures of polyol–C5–CO<sub>2</sub> (where C5 represents cyclopentane) under depressurization. The DFT was extended to consider three components. Once again, the parameters describing each component were determined by fitting a PC-SAFT model to experimental measurements of the composition at different temperatures and pressures. These measurements are described in greater detail in the following section (Section VII.3).

Using this string method model, we estimated the nucleation pathway of supersaturated PPG–cyclopentane–CO<sub>2</sub> mixtures with different weight fractions of cyclopentane. In this case, we mean the weight fraction of cyclopentane in the saturated mixture of PPG, cyclopentane, and CO<sub>2</sub>, which we will call  $w_{C5}$ . In the experiment analyzed in the previous Section,  $w_{C5} = 0.1$ . In Figure VII.3, we show

the nucleation free energy along the nucleation pathway found by the string method for  $w_{C5} = 3.5\%$ ,  $15\%$ ,  $16\%$ , and  $17.8\%$ . The polyol was modeled using the PC-SAFT parameters for PPG 2700 g/mol (see Table II.2) and was saturated with  $\text{CO}_2$  at 8 MPa and  $28^\circ\text{C}$ . The nucleation pathway was computed upon quenching the pressure to 0.1 MPa. As the weight fraction of cyclopentane increases, the peak value of the nucleation energy, the nucleation energy barrier, decreases significantly. While the nucleation barrier is about  $20 k_B T$  for  $w_{C5} = 3.5\%$ , it decreases to about  $8 k_B T$  upon increasing  $w_{C5}$  to  $15\%$ . The string method model's prediction of a significant decrease in the nucleation energy barrier upon the addition of cyclopentane is consistent with our observation of a significant increase in the nucleation rate in foaming experiments when the polyol is mixed with cyclopentane.

One possible explanation for the reduction in the nucleation barrier upon the addition of cyclopentane is the emergence of a two-stage nucleation pathway upon the addition of sufficient cyclopentane. Already at  $w_{C5} = 17.8\%$  (red line in Figure VII.3a), the nucleation pathway has two peaks, each marked with a star. The presence of two peaks along the pathway indicates that the nucleation process is split up into two stages. Because the string method finds the pathway with the lowest nucleation energy, its selection of a two-stage nucleation pathway indicates that the two stages have a lower free energy than single-stage alternatives. Those two stages appear to be a liquid–liquid phase separation followed by a vaporization of the liquid droplet, as depicted in Figure VII.3b.

We present two forms of evidence that suggest that the two stages of nucleation are liquid–liquid phase separation and vaporization. The first evidence comes from an analysis that we refer to as “incipient phase analysis.” In incipient phase analysis, we estimate the chemical potential of the mother phase immediately after quenching the pressure and solve for the composition of a phase with the same chemical potential. This phase is not in equilibrium with the mother phase because the pressures of the two phases are not set to be equal, so only chemical and thermal equilibrium are considered. Nevertheless, we propose that the composition of this phase might indicate the composition of the initial nucleus that forms upon supersaturation, even if the composition of the final phase at equilibrium is different. To estimate the chemical potential of the mother phase immediately after the pressure quench, we assume that the relative ratios of components remain fixed but allow the overall density to vary until the pressure matches the quenched pressure. Using the resulting composition, the chemical potential of the mother phase can be computed.

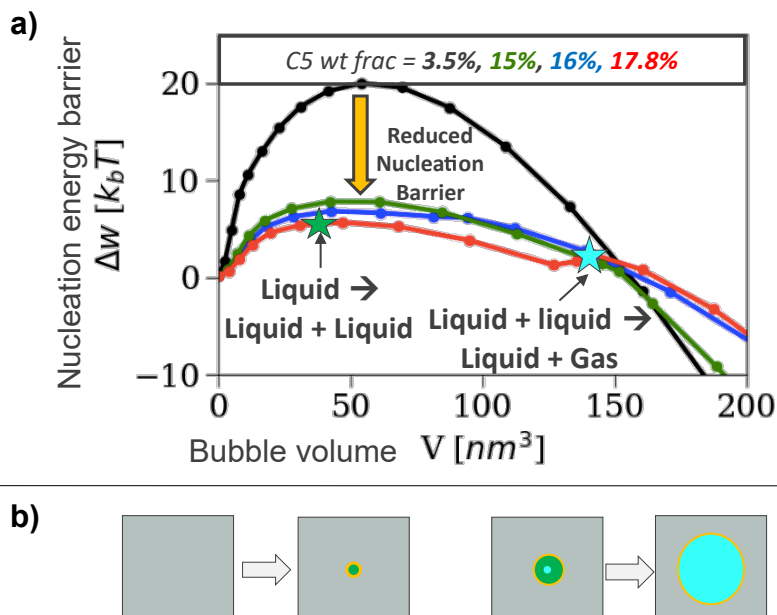


Figure VII.3: a) Nucleation energy barrier (normalized by the thermal energy  $k_B T$ ) as a function of the bubble volume (cubic nanometers) as a bubble nucleates in a mixture of 1k2f polyol (see Table II.1 for properties), cyclopentane, and  $\text{CO}_2$ . The mixture is saturated at 8 MPa and depressurized instantaneously to 0.1 MPa. The temperature is fixed at 28 °C. The string method identifies the minimum energy pathway, which is shown for four different weight fractions of cyclopentane: 3.5% (black), 15% (green), 16% (blue), and 17.8% (red). At the three highest concentrations of cyclopentane, the nucleation pathway has two peaks, meaning nucleation occurs in two stages: (1) liquid–liquid separation (dark blue star) and (2) vaporization of liquid (light blue star). b) Depiction of two stages of bubble nucleation. First, the uniform mother phase (gray) nucleates a bubble with a liquid-like density (green) surrounded by a high concentration of  $\text{CO}_2$  and cyclopentane (yellow border) through liquid–liquid phase separation. Second, the liquid-like bubble vaporizes (light blue) and grows into a larger bubble with a vapor-like density. Plot produced by Dr. Huikuan Chao.

The result of the incipient phase analysis is shown in Figure VII.4a. The grand potential density  $g$  is plotted as a function of the weight fraction of cyclopentane in the mother phase  $w_{C5}$ . The analysis identified two classes of phases that are likely to nucleate upon a pressure quench from 8 MPa to 0.1 MPa. At low weight fractions of cyclopentane, a vapor-like phase (red line) is expected. Upon reaching a sufficiently high weight fraction of cyclopentane ( $w_{C5} \approx 15\%$ ), a liquid-like phase (a phase with a liquid-like density) may nucleate (blue line). The liquid-like phase is less energetically favorable than the vapor-like phase until  $w_{C5} > 42\%$ , which is far beyond the relevant quantity for polyurethane foaming. While energetically less

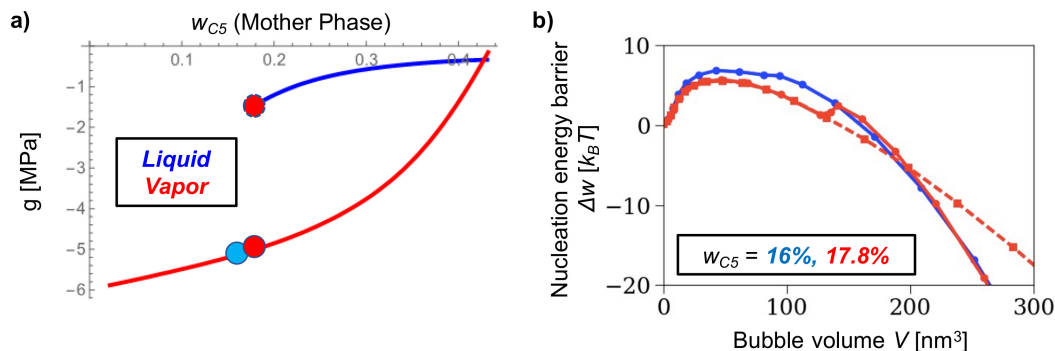


Figure VII.4: Nucleation behavior of mixtures of 1k2f polyol (see Table II.1),  $\text{CO}_2$ , and cyclopentane (C5) saturated at 8 MPa and depressurized to 0.1 MPa with temperature maintained at 28 °C. a) The free energy density of phases that can nucleate under supersaturation relative to the mother phase upon depressurization ( $g$ ), as computed using the incipient phase analysis, plotted as a function of the weight fraction of cyclopentane  $w_{C5}$  in the saturated mother phase. For  $w_{C5} < 0.17$ , only a vapor phase (red line) can nucleate. At higher  $w_{C5}$ , a liquid phase (blue line) may nucleate. While it is less energetically favorable than the vapor phase for  $w_{C5} \in [0.17, 0.43]$ , it may still nucleate by Ostwald's phase rule [10]. The blue circle corresponds to the blue line in (b). The red circle with a solid outline corresponds to the solid red line in (b) and that with the dashed outline corresponds to the dashed red line in (b). b) Nucleation energy barrier nondimensionalized by the thermal energy  $k_B T$  as a function of the bubble volume for different weight fractions of C5 (same as in Figure VII.3). The blue line ( $w_{C5} = 16\%$ ) corresponds to a single-stage nucleation of a phase with a vapor-like density. The solid red line ( $w_{C5} = 17.8\%$ ) corresponds to a two-stage nucleation of a liquid-like phase followed by a vaporization into a vapor-like phase. The dashed red line corresponds to a single-stage nucleation of a liquid-like phase. Note that the vapor-like phase of the solid red line soon becomes energetically favorable over the liquid-like phase of the dashed red line, indicating that, ultimately, a vapor-like bubble is preferred. Plots produced by Dr. Huikuan Chao.

favorable, the liquid-like phase has an energy more similar to the mother phase ( $g = 0$ ), and the Ostwald rule predicts that such a phase is the more likely to nucleate [10].

To understand the difference between the vapor-like and liquid-like routes to bubble nucleation, we plot the free energy along the nucleation pathway predicted by the string method model for both conditions in Figure VII.4b. The blue line corresponds to  $w_{C5} = 16\%$ , marked by the light blue circle in panel (a). This pathway represents nucleation directly to a vapor-like phase and has a single peak, indicating a single stage. The red line corresponds to  $w_{C5} = 17.8\%$  and has two peaks representing two stages of bubble nucleation. At this weight fraction of

cyclopentane, both vapor-like (marked by the red circle with a solid black outline in (a)) and liquid-like (marked by the red circle with a dashed black outline in (a)) phases can be formed. While the solid line in (b) represents the nucleation pathway predicted by the string method model, the dashed line represents the nucleation pathway taken if constrained to the liquid-like phase. These two pathways coincide up to the second peak, which suggests that the first peak corresponds to liquid–liquid phase separation. The pathways then diverge, with the liquid-like pathway (dashed line) having the higher free energy. While the string method model cannot be trusted beyond the peak, this discrepancy between the pathways suggests that the liquid-like bubble does not proceed with a liquid-like density. Instead, we assume that it transitions to a vapor-like density before reaching the vapor-like equilibrium phase.

The other form of evidence we present to show that the bubble undergoes liquid–liquid phase separation followed by vaporization at  $w_{C5} = 17.8\%$  is the density profiles predicted by the DFT at different stages along the nucleation pathway. A handful of these density profiles is shown in Figure VII.5 with the corresponding points along the free-energy curve indicated by red arrows. Before bubble nucleation, the system begins at a uniform composition equal to the bulk composition seen on the right of the density profile plots in Figure VII.5. Upon nucleation (see panel (i)), the nucleating phase (left of the density profile) has acquired a higher concentration of CO<sub>2</sub> (blue line) and cyclopentane (green line) and pushed out polyol (blue line), and has a liquid-like density similar to the bulk fluid. Upon reaching the first nucleation barrier (ii), the cyclopentane concentration decreases in the center of the nucleating phase and almost all the polyol is expelled. Because the density of the nucleus remains liquid-like, however, we classify this stage as liquid–liquid phase separation. The interfacial tension between two liquids is typically much smaller than at an interface between a vapor and liquid, and because the primary energetic cost is the formation of a new interface, this lower interfacial tension is likely the reason for the lower nucleation energy barrier of this stage than the single-stage nucleation into a vapor. The composition remains similar between the two nucleation energy peaks (iii), but upon reaching the second nucleation energy peak (iv), the composition of the nucleus changes dramatically. While CO<sub>2</sub> and cyclopentane remain accumulated along the bubble surface, there is almost no cyclopentane in the core of the bubble and the CO<sub>2</sub> concentration is also much lower, resulting in a vapor-like density at the core. This vapor-like region expands beyond the second peak (v), so we classify this stage as the vaporization of the liquid bubble. Therefore,

we suggest that one reason why adding cyclopentane to the polyol dramatically increases the nucleation rate is that it can phase separate into a metastable liquid-like phase with CO<sub>2</sub> before vaporizing, which requires less energy than nucleating a vapor-like phase all at once.

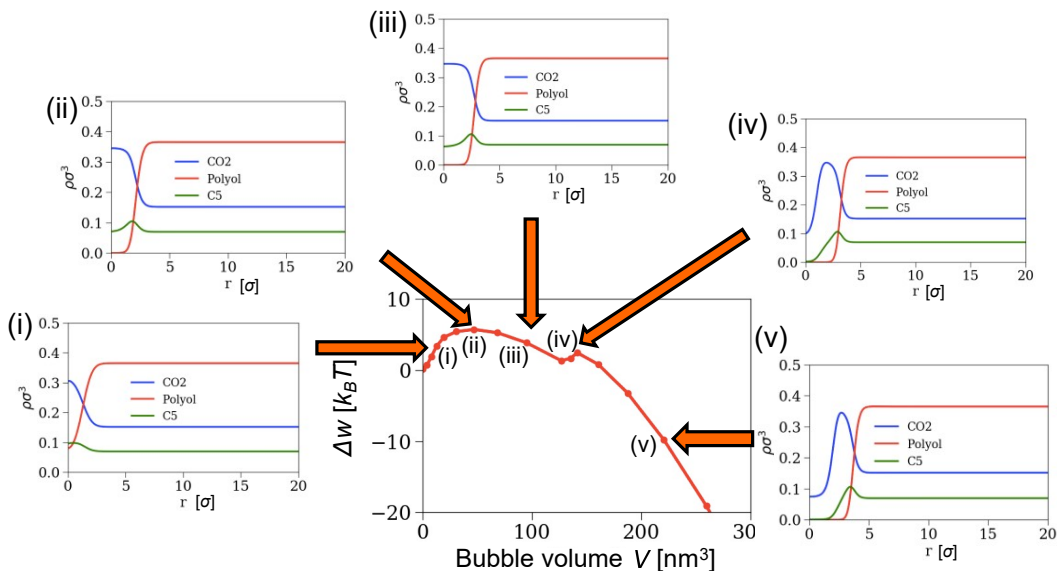


Figure VII.5: Center) Nucleation barrier in units of  $k_B T$  as a function of the bubble size for a mixture of 1k2f polyol (see Table II.1), CO<sub>2</sub>, and cyclopentane (C5) saturated at 8 MPa and depressurized to 0.1 MPa with temperature maintained at 28 °C, with initial C5 weight fraction of 17.8% (red line in Figures VII.3a and VII.4b). Around the nucleation barrier, the density profiles of the three components (CO<sub>2</sub> in blue, polyol in red, and cyclopentane (C5) in green) are plotted for different points along the nucleation pathway, indicated by orange block arrows. The densities are given in units of number of molecules per CO<sub>2</sub> bead diameter cubed ( $\sigma^{-3}$ ), and the radius measured from the center of the nucleus  $r$  is given in units of the CO<sub>2</sub> bead diameter  $\sigma$  ( $\sigma = 2.79$  Å as shown in Table II.2). Before the second peak, the total density of the nucleating phase (small  $r$ ) is similar to the mother phase ( $\approx 0.5$  vs.  $\approx 0.6$ ), indicating a liquid-like embryo. Upon reaching the second peak (fourth plot of density profiles), the density at the core of the bubble embryo significantly decreases to about 0.1, indicating a vaporization to a vapor-like bubble, after which, the bubble grows while maintaining a roughly constant core density. Plots produced by Dr. Huikuan Chao.

This particular two-stage nucleation pathway has only been proposed theoretically for bubble nucleation; other factors may cause the increased bubble nucleation in formulations with cyclopentane. One possible alternative explanation for the enhancement of bubble nucleation upon the addition of cyclopentane was phase separation of cyclopentane into small droplets that provide additional nucleation sites. Similar droplets have been observed with SEM in polyurethane foams upon

the addition of isopentane to a polyol formulation [12], which has an even lower boiling point than cyclopentane (27.8 °C for isopentane vs. 49.2 °C). While light scattering could have revealed the presence of phase-separated microdroplets in the polyol–cyclopentane–CO<sub>2</sub> mixture, we examined the solubility of cyclopentane through another approach. First, we mixed cyclopentane with polyol under atmospheric pressure to determine its solubility. We found that cyclopentane is miscible at least up to 50% by weight in 1k2f polyol (see Table II.1, which is similar to the 3k2f polyol (PPG 2700 g/mol) used in this experiment, but with a lower molecular weight (the difference in molecular weight means cyclopentane is less soluble in 3k2f, but not significantly less so). Therefore, we only mixed in 17% cyclopentane by weight, well below the solubility. Second, we maintained the conditions far from those that lead to a three-phase coexistence at which cyclopentane-rich droplets will phase separate. These conditions are explored in the next Section.

### **VII.3 Adding Cyclopentane Opens Up Three-phase Region**

*First, see Section VII.S1 for some information on safety precautions to take when performing experiments with cyclopentane.*

Why should the addition of cyclopentane open up a two-stage nucleation pathway with such a low nucleation barrier? We propose that the result is rooted in the thermodynamics of the mother phase, which we show reaches a three-phase coexistence under similar conditions. As shown by Müller *et al.*, under conditions near a three-phase coexistence, depressurization can drive the nucleation of bubble embryos whose surfaces are wetted by a solvent-rich liquid phase that may condense into a liquid-like phase in the bubble interior, just as is predicted by the string method to form in the first stage of bubble nucleation (Section VII.2). This partial condensation reduces the interfacial tension along the bubble surface relative to a vapor-like bubble, which reduces the nucleation energy barrier. While not thermodynamically favorable (see Figure VII.4), this liquid-like phase may still be preferred during nucleation because its free energy is more similar to that of the mother phase, as predicted by Ostwald's rule [10]. In this Section, we provide experimental evidence of a three-phase coexistence in the vicinity of the foaming conditions explored in Section VII.1 and fit the parameters of a PC-SAFT model for a three-component system to estimate the extent of this region. The parameters of this model also serve as the parameters of the DFT model that forms the basis of the string method used to predict the two-stage nucleation pathway in Section VII.1.

Tompa first presented a prediction that ternary mixtures of polymer, solvent, and vapor could yield a three-phase coexistence within a particular range of temperatures, pressures, and compositions [6], which Sundar and Widom elaborated upon [13]. Models have since been developed to predict the parameter range of three-phase coexistence in specific polymer–solvent–gas mixtures relevant to industrial processes, such as supercritical CO<sub>2</sub> extraction of solvent from polymer [7, 14]. Experimental measurements demonstrating three-phase coexistence are scarce, however. Most use some combination of cloud-point measurements—which can be imprecise and hysteretic for viscous polymers—and painstaking analysis of the compositions for each sample of polymer-containing phases [15, 16]. Bungert *et al.* showed a three-phase coexistence in a ternary mixture of polystyrene, cyclohexane, and CO<sub>2</sub>, but at much higher temperature (170 °C) than is relevant for bubble nucleation in polyurethane foaming [15]. Nevertheless, we cannot be sure that a three-phase coexistence will occur for this mixture without measurement, and we cannot have confidence about the window of parameters that permit it without theory.

Before performing an experiment, however, we extended the two-component PC-SAFT model to treat three-component mixtures of polyol, CO<sub>2</sub>, and cyclopentane. We determined the cyclopentane parameters by fitting a two-component model of cyclopentane and CO<sub>2</sub> to literature data on their binary phase coexistence [17, 18]. Because we could not obtain accurate measurements of the solubility of cyclopentane in polyol, we assumed that the interaction parameter  $k$  between polyol and cyclopentane was the same as that between CO<sub>2</sub> and polyol. We tested this crude approximation against experimental results shown later in this Section.

With the PC-SAFT model extended to ternary mixtures of polyol, CO<sub>2</sub>, and cyclopentane, we could predict the conditions that might support a three-phase coexistence. These predictions are best presented on a Gibbs triangle, which we explain in Figure VII.6.

After searching through a range of pressures and temperatures, we found that the ternary PC-SAFT model predicted a three-phase coexistence at 37 °C and 6.7 MPa, as shown in Figure VII.7. Four types of phase coexistence are possible under these conditions, and a three-phase coexistence is only possible within a small range of compositions. First, a single-phase coexistence is predicted in the unmarked region at low concentrations of CO<sub>2</sub> (bottom of Gibbs triangle). At higher concentrations of CO<sub>2</sub> and lower concentrations of cyclopentane, a vapor–

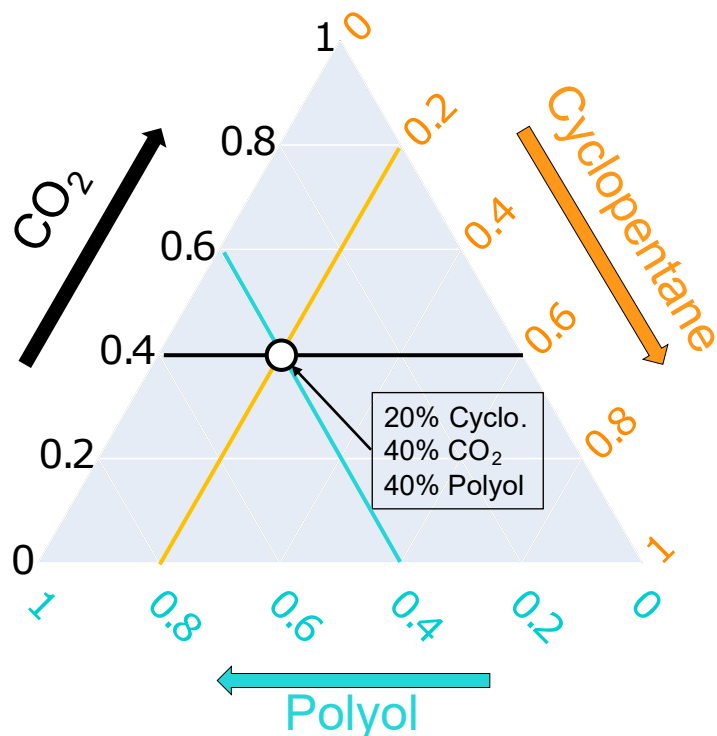


Figure VII.6: A Gibbs triangle is shown for indicating the weight fractions of each compound in a mixture of CO<sub>2</sub> (black, left axis), cyclopentane (gold, right axis), and polyol (light blue, bottom axis). A point (white circle) is plotted indicating a mixture with a composition of 20 % cyclopentane, 40 % CO<sub>2</sub>, and 40 % polyol. Three lines indicating the corresponding composition of each phase are drawn intersecting the point.

liquid equilibrium (VLE) is possible between an almost purely CO<sub>2</sub> phase (upper tip of Gibbs triangle) and a polyol-rich, cyclopentane-poor liquid phase (bottom black line). Upon adding enough CO<sub>2</sub> and cyclopentane to enter the orange triangular region on the phase diagram, the system is predicted to separate into three phases, marked with stars: a CO<sub>2</sub>-rich vapor (blue star), a polyol-rich liquid (green star), and a liquid-like phase of CO<sub>2</sub> and cyclopentane (pink star). For example, if the system composition were that indicated by the white circle in the Figure, it would separate into compositions marked by the three circles according to conservation of mass. Finally, at still higher concentrations of cyclopentane, the system is predicted to reach a liquid–liquid equilibrium (LLE), at which point the CO<sub>2</sub>-rich vapor phase condenses into the liquid of CO<sub>2</sub> and cyclopentane.

Directly preparing a system with a composition in the three-phase region of Figure VII.7 at the pressure and temperature required can be challenging. Based on the PC-SAFT predictions of phase behavior, however, the system should pass

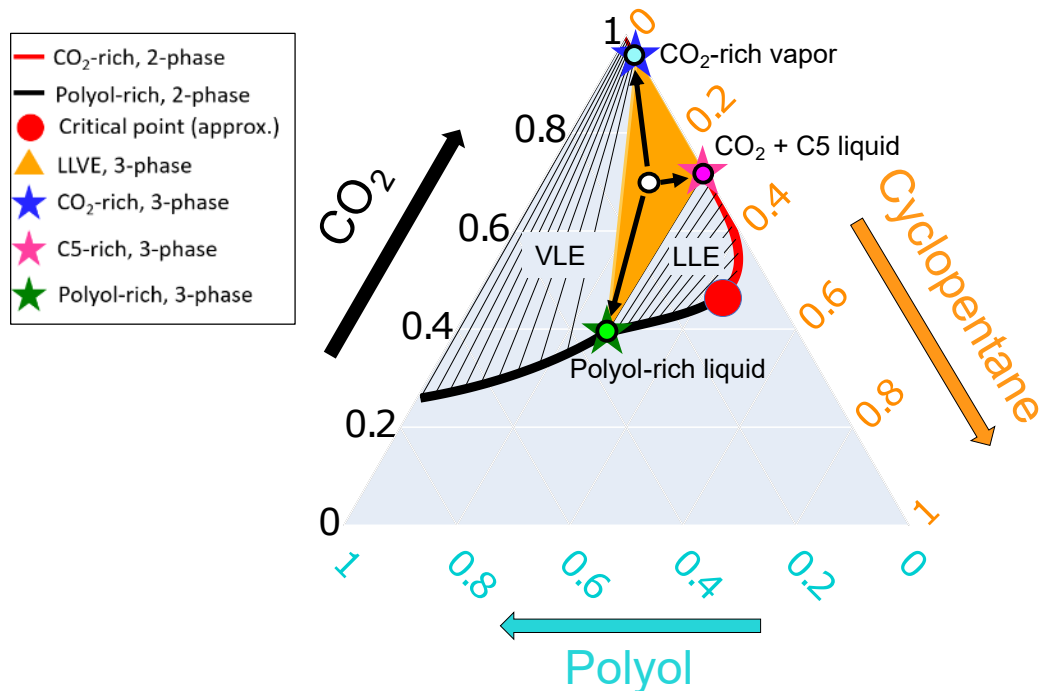


Figure VII.7: Prediction by PC-SAFT model of phase behavior of ternary mixture of 1k2f polyol (see Table II.1),  $\text{CO}_2$ , and cyclopentane at 6.7 MPa and 37 °C. In the left region of the Gibbs triangle, at low cyclopentane concentrations, the system achieves a vapor–liquid equilibrium (VLE) between a  $\text{CO}_2$ -rich vapor (red line near the top) and a polyol-rich liquid (black line). Tie lines are marked in between coexisting phases. In the right region, at high cyclopentane concentrations, the system achieves a liquid–liquid equilibrium (LLE) between a liquid of  $\text{CO}_2$  and cyclopentane (red line) and a polyol-rich liquid (black line) with tie lines drawn between. At high enough cyclopentane concentrations, the system reaches a critical point (general location indicated by red circle) before becoming a single phase (lower region of Gibbs triangle). At intermediate concentrations of cyclopentane, the system achieves a liquid–liquid–vapor equilibrium (LLVE, orange triangle) among a  $\text{CO}_2$ -rich vapor (blue star), polyol-rich liquid (green star), and liquid of  $\text{CO}_2$  and cyclopentane (pink star). If a system is prepared with the concentration indicated by the white circle, it separates into three phases with concentrations indicated by the light blue, light green, and pink circles consistent with mass conservation.

through the three-phase coexistence simply by pressurizing a vessel in gradual steps with  $\text{CO}_2$ , as shown in Figure VII.8. Therefore, to probe the possibility of a three-phase coexistence, we pressurized a Parr reactor filled with cyclopentane and polyol with  $\text{CO}_2$  in steps. At low pressure (2.2 MPa), the system should only exist in a vapor–liquid equilibrium. Both phases can be sampled by the sampling apparatus, so this stage can be validated by comparing the sampled compositions to the predicted compositions. Upon adding  $\text{CO}_2$  to reach higher pressure (7.0 MPa),

a three-phase coexistence opens up and the system will pass through it. At this point, the sampled compositions should match the liquid and vapor phases of the three-phase coexistence, but they will not account for all the mass in the system, some of which will be in the third phase of intermediate density (pink). Upon adding more  $\text{CO}_2$  to reach still higher pressures (8.0 MPa), the system will reach a liquid–liquid equilibrium, at which point the gas-sampling valve should sample a liquid phase rather than a vapor phase.

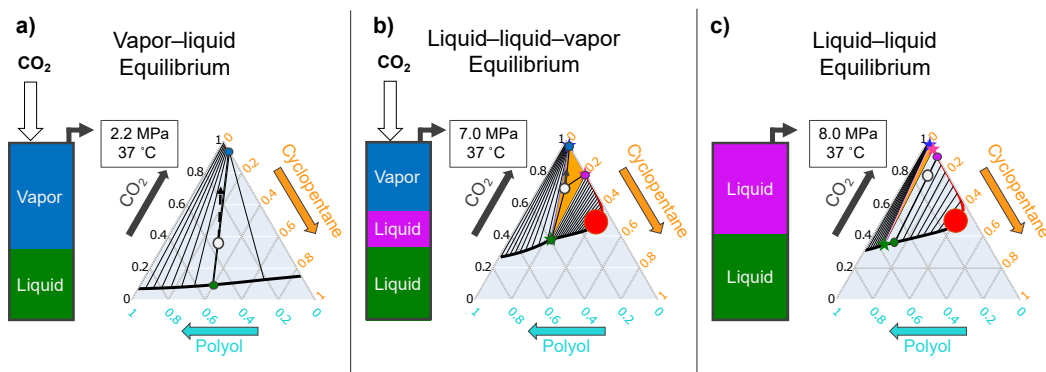


Figure VII.8: Schematic of experimental plan for demonstrating a liquid–liquid–vapor equilibrium by passing through three qualitatively distinct phase regimes simply by adding  $\text{CO}_2$ . In each panel, the high-pressure vessel is indicated by a vertical rectangle on the left with the predicted phase composition indicated. After sampling the composition of each phase in the mixture (indicated by green, blue, and pink circles in the theoretical phase diagram on the right),  $\text{CO}_2$  is added (indicated by white block arrow), which raises the  $\text{CO}_2$  weight fraction in the overall composition (white circle with increased  $\text{CO}_2$  indicated by dashed arrow) and the pressure to reach the condition in the next panel to the right. Temperature is fixed at 37 °C for simplicity. a) vapor–liquid equilibrium (VLE) at 2.2 MPa, b) liquid–liquid–vapor equilibrium (LLVE) at 7.0 MPa, and c) liquid–liquid equilibrium (LLE) at 8.0 MPa.

To demonstrate three-phase coexistence in a mixture of polyol, cyclopentane, and  $\text{CO}_2$ , we developed a novel, high-pressure, gas- and liquid-sampling apparatus. The apparatus was constructed at the TXINN Research Facility at Dow, Inc. in Lake Jackson, TX. Its design and method of operation are discussed below.

### High-pressure Liquid- and Gas-phase Sampling

The primary challenge of demonstrating a three-phase coexistence is to sample each phase at high pressure. This task requires that sampled volumes are small, increasing the variability, and that the components in the sample come out at high pressure. We developed a unique approach to estimate the composition of each phase by sampling only the liquid and vapor phases and using conservation of

mass to estimate the composition of any intermediate-density third phase that might phase separate. A schematic of the apparatus is shown in Figure VII.9.

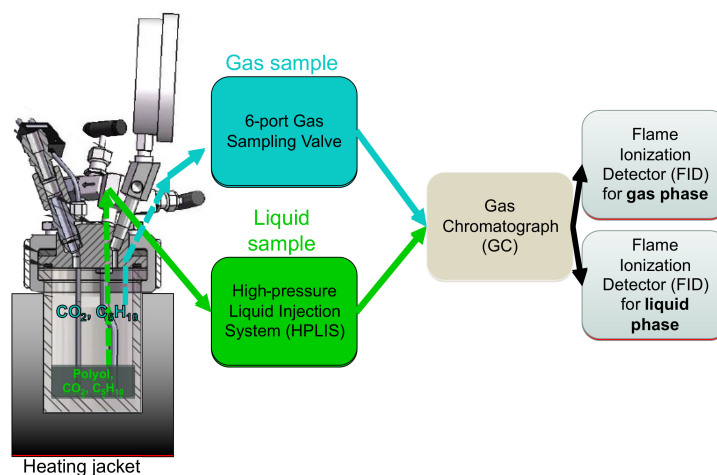


Figure VII.9: On the left, a Parr reactor (image obtained from the Parr Instrument Company's operating instruction manual of 4600 & 4700 models) contains a mixture of polyol, cyclopentane ( $C_5H_{10}$ ), and polyol that has phase-separated into a denser phase (darker region at bottom) and polyol-free lighter phase. A heating jacket (black) surrounds it to maintain the temperature. The gas-like lighter phase is sampled from the gas-sampling valve (following the path of the blue arrows) at the top of the Parr reactor and flowed through a 6-port gas-sampling valve, which collects a small volume of that gas under pressure and sends it to a gas chromatograph (GC). The liquid-like denser phase is sampled from a dip tube (following the path of the green arrows) to a high-pressure liquid injection system (HPLIS), which vaporizes the  $CO_2$  and cyclopentane and flows them to the same GC. Inside the GC, effluent from the gas and liquid samples are flowed through separate columns to separate flame ionization detectors (FIDs) with methanizers that measure the cyclopentane and  $CO_2$  content.

The ternary mixtures of PPG 2700 g/mol, cyclopentane, and  $CO_2$  were equilibrated in 1.2 L Parr reactor and are sampled from both the top through the gas-sampling port and the bottom through a dip tube. The headspace sample flows directly through a gas-sampling valve that is connected to the gas chromatograph (GC) at atmospheric pressure. The dense phase sample flows through a heated high-pressure liquid injection system (HPLIS), which vaporizes the volatile  $CO_2$  and cyclopentane out of the polyol before flushing these volatile components into the GC. The polyol composition is not directly measured; see Section VII.S3 in the SI for the method for estimating the polyol density in the liquid sample. The samples are prepared by first dissolving cyclopentane in polyol at roughly 50% by weight and adding the solution to the Parr reactor inside a nitrogen-atmosphere glovebox,

which reduces the risk of flammability. During the experiment, CO<sub>2</sub> is added at high pressure using an ISCO pump, which is fed through a dip tube from a liquid CO<sub>2</sub> tank. The temperature is controlled using a temperature-control jacket around the Parr reactor. The components can be mixed using the mixing head built into the Parr reactor. Dead volumes were kept small to minimize loss of the contents of the Parr reactor when flushing the sampling valves to take a new measurement. A photo of the completed apparatus is shown inside a walk-in hood in Figure VII.10.

For details on the validation of the experimental method and data analysis, see the SI.

One major limitation of this design is that it cannot directly sample a third phase of intermediate density because it separates in between the low-density CO<sub>2</sub>-rich phase and the high-density polyol-rich phase under the force of gravity, and we do not have a sampling port in that region (see Figure VII.11). We explore an indirect method for demonstrating the formation of such a third phase below.

### **Demonstration of Three-phase Coexistence**

Following the plan outlined in Figure VII.8, we pressurized the vessel in steps and sampled the light and dense phases. The sample prepared in the Parr reactor was composed of 84 g PPG (2700 g/mol) and 79 g cyclopentane (48.5% by weight cyclopentane, which appeared to be soluble at room temperature). The total volume of 188 mL had a depth of 3.5 cm inside the 1.2 L Parr reactor chamber. The sample was kept at a temperature of  $37 \pm 4$  °C by a heating jacket around the Parr reactor and mixed at 10 RPM between measurements. The phase behavior was changed by injecting CO<sub>2</sub> as outlined in Figure VII.8.

The compositions of the dense liquid phase and headspace were measured after each injection of CO<sub>2</sub>. These compositions, along with the estimate of the overall composition (see Section VII.S3 for details of analysis), are plotted in Figure VII.12. The overall composition (white circles) increases in CO<sub>2</sub> concentration toward the CO<sub>2</sub> vertex after each injection (indicated by white arrow). The headspace composition (blue circles, see zoomed in CO<sub>2</sub> vertex on the right) initially increases in CO<sub>2</sub> concentration toward the CO<sub>2</sub> vertex as well. Upon increasing the pressure from 6.7 MPa to 7.0 MPa, however, the CO<sub>2</sub> weight fraction remained roughly constant. Upon increasing the pressure from 7.0 MPa to 7.5 MPa, the CO<sub>2</sub> weight fraction actually decreased (indicated by dark blue arrow). In the liquid phase sample (green circles), the addition of CO<sub>2</sub> likewise initially increased the CO<sub>2</sub>

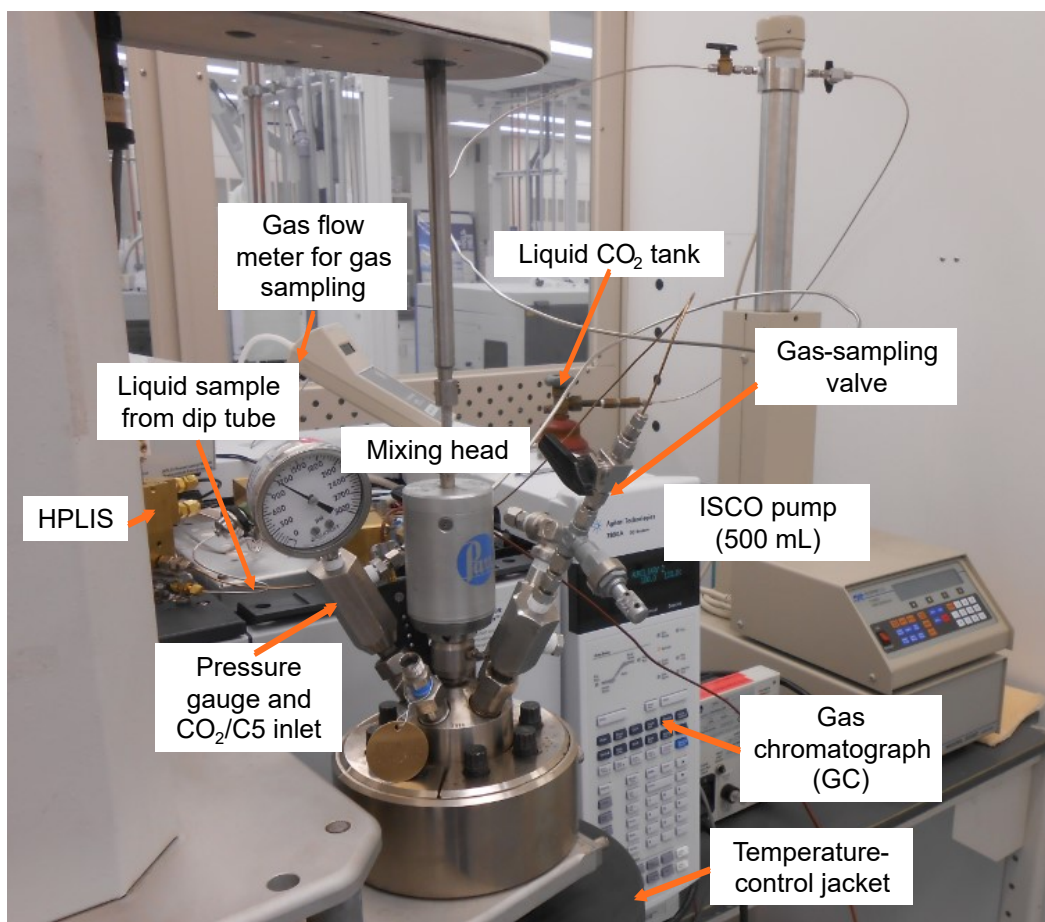


Figure VII.10: Image of the high-pressure sampling apparatus built at the TXINN facility at Dow, Inc., Lake Jackson, TX, based on the schematic in Figure VII.9. In the front left, a Parr reactor fixed into a mixing apparatus and temperature-control heating jacket holds the high-pressure mixture. Pressure is indicated by a pressure gauge attached to the inlet. The inlet is supplied with CO<sub>2</sub> or cyclopentane by a high-pressure ISCO syringe pump shown on the right, which receives liquid CO<sub>2</sub> from a tank in the back. The gas-like light phase is sampled through the valve on the right of the Parr reactor, from which it passes through a gas-sampling valve (not visible). A small sample then is flowed into the gas chromatograph (GC) and out through a gas flow meter. The liquid sample collected from the bottom of the dip tube of the Parr reactor passes through the tubing indicated into the high-pressure liquid injection system (HPLIS), from which the vaporized CO<sub>2</sub> and cyclopentane flow into the GC (see Figure VII.S1 for alternative perspective). The apparatus is contained within a walk-in hood as an added safety measure in the unlikely scenario of the release of the pressurized contents.

composition. Upon increasing the pressure from 6.7 MPa to 7.0 MPa, the CO<sub>2</sub> weight fraction remained constant, the cyclopentane weight fraction decreased, and the polyol weight fraction increased. This trend continued upon increasing the

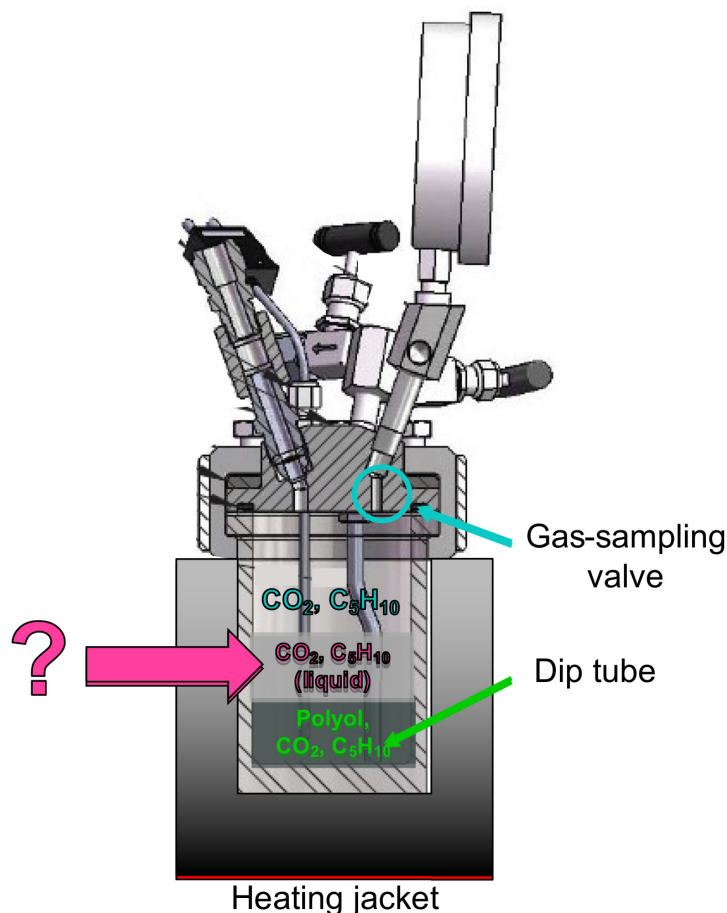


Figure VII.11: A schematic of a three-phase coexistence in a high-pressure mixture of polyol, CO<sub>2</sub>, and cyclopentane (C<sub>5</sub>H<sub>10</sub>) in a Parr reactor (image obtained from the Parr Instrument Company's operating instruction manual of 4600 & 4700 models) with temperature maintained by a heating jacket (black). The dense, liquid-like phase of polyol, CO<sub>2</sub>, and C<sub>5</sub>H<sub>10</sub> can be sampled by the dip tube that extends almost to the bottom of the Parr reactor (green). The light, gas-like phase of CO<sub>2</sub> and C<sub>5</sub>H<sub>10</sub> can be sampled by the gas-sampling valve at the top of the chamber (light blue). The intermediate, liquid-like phase of CO<sub>2</sub> and C<sub>5</sub>H<sub>10</sub> cannot be sampled (pink), so its composition is not directly measurable.

pressure from 7.0 MPa to 7.5 MPa after another injection of CO<sub>2</sub>.

These anomalous changes in the composition of both liquid and vapor phases appear to violate the conservation of mass—how can the weight fraction of CO<sub>2</sub> decrease (vapor phase) or remain constant (liquid phase) upon adding CO<sub>2</sub>? We suggest that the missing CO<sub>2</sub> has formed part of a CO<sub>2</sub>-rich third phase of intermediate density, which cannot be sampled (as shown in Figure VII.11).

While the anomalous changes in composition upon injecting the Parr reactor

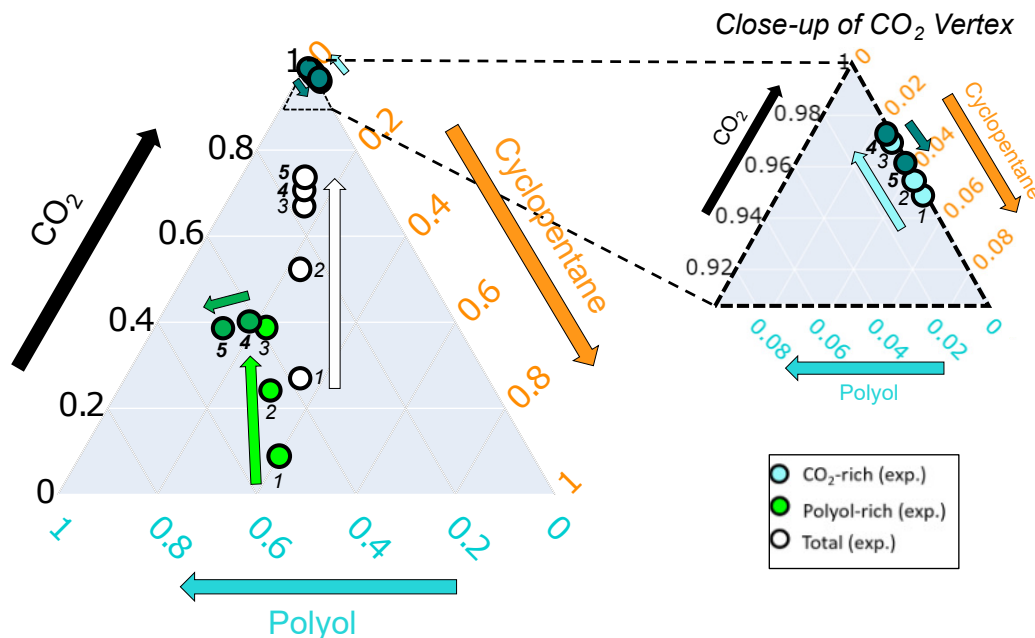


Figure VII.12: The composition of the overall system (white circle), sampled polyol-rich dense liquid phase (light and dark green circles), and sampled  $\text{CO}_2$ -rich light gas phase (light and dark blue circles) are plotted on a Gibbs triangle at 5 pressures: (1) 2.2 MPa, (2) 5.0 MPa, (3) 6.7 MPa, (4) 7.0 MPa, and (5) 7.5 MPa. Temperature is fixed at 37 °C. The region near the  $\text{CO}_2$  vertex at the top is shown in greater detail on the right to distinguish the composition of the sampled  $\text{CO}_2$ -rich phase. While the overall  $\text{CO}_2$  content increases (white circles), the  $\text{CO}_2$  content plateaus at 0.4 in the polyol-rich phase (dark green circles) and decreases in the  $\text{CO}_2$ -rich phase (dark blue circles), suggesting that  $\text{CO}_2$  is lost to the formation of a  $\text{CO}_2$ -rich third phase.

with  $\text{CO}_2$  provide evidence for the formation of a third phase, it does not provide information about the validity of the PC-SAFT model that predicted a third phase under those conditions. To validate the PC-SAFT model quantitatively, we compared the measured and predicted compositions of liquid and vapor phases. The model was generally in agreement, but we only compare the theoretical predictions to one measurement taken at 7.5 MPa and 37 °C for brevity in Figure VII.12a. The measured compositions are plotted as circles outlined in black: the white circle represents the overall composition, the green circle represents the measured headspace composition, and the blue circle represents the measured liquid-phase composition. The overall composition (white circle) is in the range of compositions that the PC-SAFT model predicts will phase separate into three coexisting phases. The headspace composition (blue circle) closely matches the predicted composition of the  $\text{CO}_2$ -rich vapor-like phase (blue star; see zoomed in  $\text{CO}_2$  vertex to the left). Likewise, the liquid-phase composition (green circle) closely matches the predicted

composition of the polyol-rich liquid-like phase (green star). While not shown, the densities are also in good agreement.

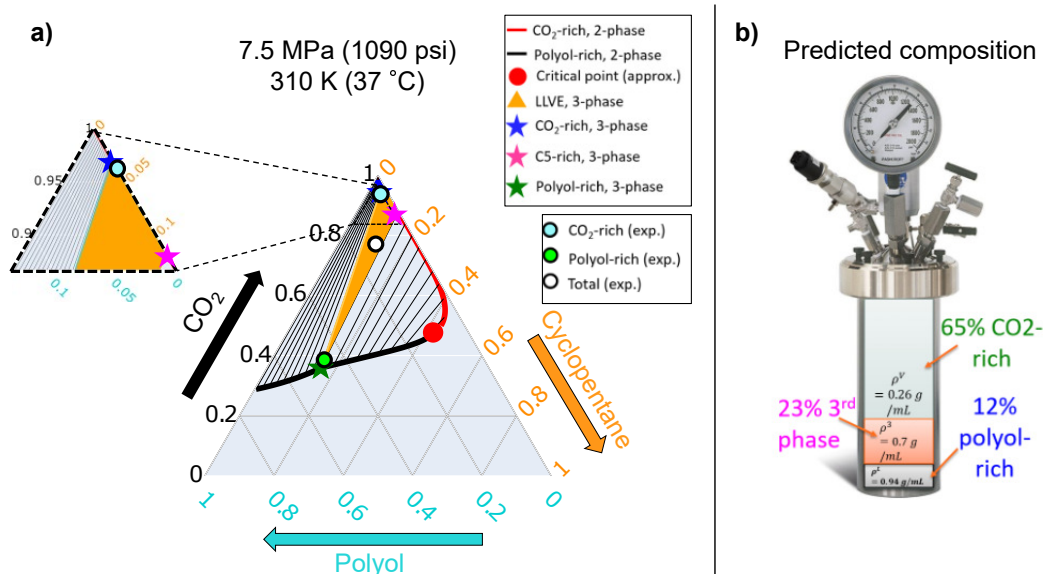


Figure VII.13: a) Measured composition (overall: white circle, CO<sub>2</sub>-rich gas: blue circle, and polyol-rich liquid: green circle) superimposed on the PC-SAFT prediction of the phase diagram (see Figure VII.7 for details) at 7.5 MPa and 37 °C. The measured compositions are consistent with a three-phase coexistence, although the third phase (pink star) is not directly measured. b) Estimated volume and density of each phase depicted inside the Parr reactor (image obtained from <https://www.parrinst.com/products/stirred-reactors/>).

The overall composition does not lie along a tie line between the liquid and vapor compositions, however, indicating that a third phase must have formed to satisfy conservation of mass. To estimate the volume of this third phase relative to the other phases, we estimate the mass of cyclopentane that would be “missing” from the sample if such a third phase did not exist. To estimate this missing mass, we first measure the density of cyclopentane in the liquid  $\rho_{C5}^L$  and vapor  $\rho_{C5}^V$  phases. Next, we estimate the volume of the liquid phase  $V^L$  by assuming that all the polyol in the sample is in the liquid phase (because the vapor pressure is too low to be appreciably present in the vapor phase). Thus,

$$V^L = \frac{m_{poly}}{\rho_{poly}^L} \quad (\text{VII.1})$$

where  $m_{poly}$  is the mass of polyol in the original sample (84 g)  $\rho_{poly}^L$  is the density of polyol in the liquid phase predicted by the PC-SAFT model. Next, we predict the

mass of cyclopentane assuming only a liquid and a vapor phase,

$$m_{C5}^{pred} = (V - V^L)\rho_{C5}^V + V^L\rho_{C5}^L \quad (\text{VII.2})$$

where  $V$  is the internal volume of the Parr reactor (1200 mL) and  $V - V^L$  is our estimate of the vapor phase density (because we assumed that there were only two phases).

We then compare this prediction for the mass of cyclopentane in the Parr reactor with the amount that should be remaining after sampling. We know the initial amount  $m_{C5}^0 = 78.5$  g. By estimating the volume of each liquid sample and multiplying it by the measured density of cyclopentane, we can estimate how much is lost after  $N$  samples,

$$m_{sample}^N = \sum_{i=1}^N \rho_{C5,i}^L V_i^{sample} \quad (\text{VII.3})$$

The remaining cyclopentane after  $N$  samples is then  $m_{C5}^N = m_{C5}^0 - m_{sample}^N$ . The missing cyclopentane is then  $m_{C5}^{missing} = m_{C5}^0 - m_{C5}^N$  and is assumed to have formed a third phase if the value is non-negligible. The volume of the third phase can then be estimated by dividing the mass of cyclopentane in the third phase by the density of cyclopentane in that phase predicted by PC-SAFT (pink star),  $V^{(3)} = m_{C5}^{missing} / \rho_{C5}^{(3)}$ , where a superscript (3) represents the third phase.

### Three-phase Coexistence Can Be the Door to Low-barrier Nucleation

As discussed in the introduction to this Chapter, proximity on the phase diagram to a three-phase coexistence often opens up a two-stage nucleation pathway [8, 9]. Indeed, we observed a significant increase in the bubble nucleation rate upon the addition of cyclopentane to the foaming fluid while also demonstrating that a three-phase coexistence can be achieved in such a fluid, although under somewhat different conditions (higher temperature and higher cyclopentane fraction). Furthermore, we showed with our string method model a probable pathway to nucleation through two stages: liquid–liquid phase separation followed by vaporization. Such two-stage nucleation occurs rapidly and nuclei remain in the liquid-like state for fleetingly brief periods of time because it is metastable. Our PC-SAFT model has shown, however, that a liquid-like phase of cyclopentane and  $\text{CO}_2$  can be thermodynamically stable under some conditions. Here, we propose using such conditions

to drive low-barrier liquid–liquid phase separation followed by depressurization to drive the formation of vapor-like bubbles, as shown in Figure VII.14b. To stabilize the liquid phase, we heat the sample from 22 °C to 42 °C while maintaining the pressure at 8 MPa. This heating shifts the phase boundary such that the most stable phase behavior of a solution prepared with a composition of 40% polyol, 40% CO<sub>2</sub>, and 20 % cyclopentane changes from a single phase to a liquid–liquid equilibrium. The liquid droplets that separate out of solution at this higher temperature will be thermodynamically stable aside from a drive to coalesce, which is reduced due to the low interfacial tension around liquid-like droplets. The low interfacial tension would also reduce the nucleation energy barrier, similar to the lower nucleation energy barrier for producing the metastable liquid phase predicted by the string method model and shown in Figure VII.4. We hypothesize that much more liquid droplets could be nucleated in this way than by a single-step nucleation into the vapor phase due to this lower nucleation barrier. The liquid-like droplets can then be vaporized by depressurizing the system to atmospheric pressure, which may also nucleate more vapor bubbles in the bulk if there is enough dissolved gas remaining.

#### **VII.4 Future Work**

Starting from this foothold, we intended to add in each of the key components in a polyurethane formulation—physical blowing agent, surfactant, isocyanate, heat, water, and catalyst—one at a time. Due to the complexity of the experiment, we have only just begun this process by exploring the effects of adding cyclopentane, just one common physical blowing agent used in polyurethane foaming. Exploring the effects of adding the remaining components of a complete polyurethane formulation in different combinations is therefore left to future work.

The next immediate step to explore would be to add surfactant to a mixture of polyol and CO<sub>2</sub>. The effect of surfactant on polyurethane foaming has been explored before by Minogue [19], who found that surfactant reduces cell diameter in the final foam (see Fig. 3-25 in [19]). Minogue, however, suggests that the surfactant only stabilizes bubble nuclei and does not actually affect the nucleation process. This idea could be tested with the present apparatus by applying the techniques described in Chapters VI and VII to estimate the nucleation rate at different degrees of supersaturation. The apparatus could also watch the process of ripening and coalescence (ripening seems to be most common—see Chapter VIII) to see how its time scale is affected by the presence of surfactant. Additionally, these experiments could test recent findings of the favorability of nucleating bubbles from surfactant

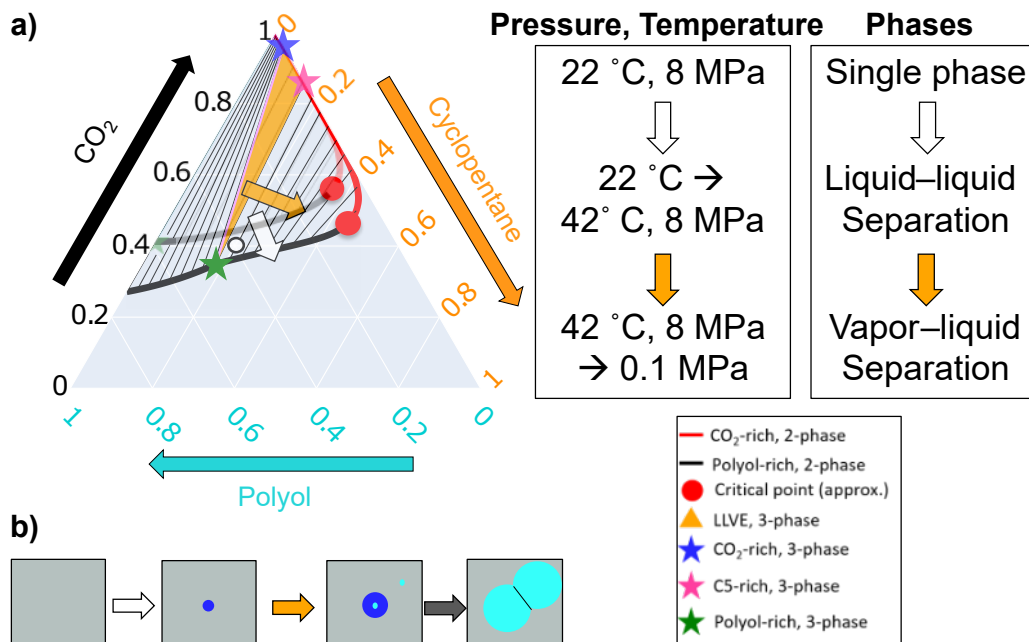


Figure VII.14: Depiction of method of two-stage foaming to enhance bubble nucleation. a) Predicted phase behavior. First, a mixture is prepared at low temperature (22 °C) and high pressure (8 MPa) at a composition that is predicted to form a single phase. The mixture is then heated to 42 °C, which widens the two-phase region enough that the mixture undergoes liquid–liquid phase separation, driving the formation of small, liquid-like bubbles with a low nucleation energy barrier due to the low interfacial tension. Finally, the mixture is depressurized to atmospheric pressure, causing the vapor–liquid equilibrium to widen and drive both the vaporization of the liquid-like bubbles and, if any excess CO<sub>2</sub> and cyclopentane remain, new vapor-like bubbles. b) Schematic of liquid–liquid phase separation followed by vaporization of liquid bubbles and nucleation of new vapor-like bubbles, which grow until they meet and form the cells of the foam.

micelles that form in ternary mixtures of polyol, PEO–PDMS surfactant, and CO<sub>2</sub> explored by our collaborator Dr. Sriteja Mantha (publication forthcoming).

A key component of polyurethane not explored in the present thesis is isocyanate. Without isocyanate, polyurethane cannot be produced. We did not perform experiments with isocyanate in the present work due to the complexity of its reaction and its high hazard as a sensitizer. The proper application of the work of this thesis to polyurethane foaming will require experiments involving isocyanate. Reacting isocyanate with a polyol formulation directly makes the isolation of the effects of the many simultaneous processes occurring during the reaction challenging. These processes are cross-linking, exothermic release of heat, generation of CO<sub>2</sub> upon reaction with water, and an advancing reaction front [20]. Isolating each of these

individually may not be possible, but we suggest a sequence of conditions to test before considering the complete polyurethane reaction to distinguish their effects more clearly in Figure VII.15.

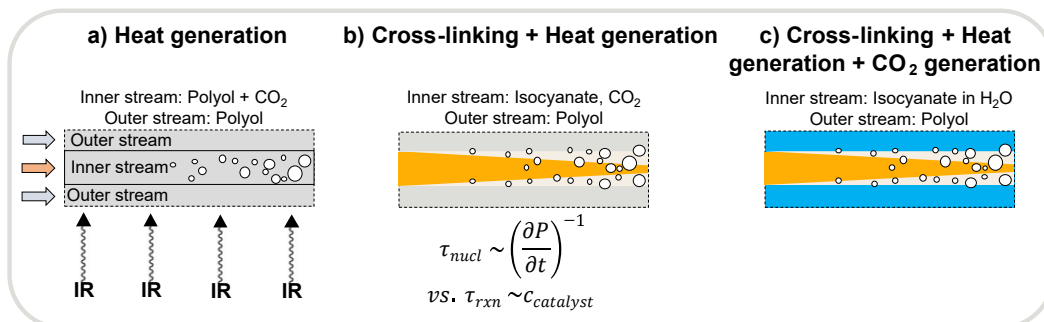


Figure VII.15: Sequence of experiments proposed for studying the effects of isocyanate on bubble nucleation in polyurethane foaming. In each diagram, a zoomed-in section of the sheath flow is shown. The flow enters from the left and exits to the right (see arrows on the left of (a)). The inner stream is at the center and sheathed by the outer stream at the top and bottom of the schematic images. The outer stream appears smaller than the inner stream because it is only partially shown—in general, the inner stream is significantly narrower than the outer stream. Bubbles are indicated by white circles of varying size. a) Focus on the effect of heat generation that would result from the exothermic reaction of isocyanate and polyol. The effect of heat can be decoupled from reaction by heating the inner stream directly, such as by infrared lamps. b) Add the effect of cross-linking to the effect of heating by studying the reaction of isocyanate with dissolved  $\text{CO}_2$  inside an outer stream of polyol in the absence of water, which would generate  $\text{CO}_2$ . The time scale of the polyurethane synthesis reaction could be varied by the adjustment of the catalyst dissolved in the polyol phase. c) The full polyurethane synthesis reaction can be studied by adding water to the polyol phase (indicated by blue color of the polyol in the outer stream), which reacts with isocyanate to generate  $\text{CO}_2$  *in situ*.

The effect of heat on bubble nucleation and growth can be studied independently of the isocyanate reaction. The same experiments as have been presented in the present thesis can be repeated while heating the inner stream to test this effect. Heat could be supplied by an infrared light source directed at the inner stream (keeping in mind the limited transmission of infrared by the quartz capillary). Heat could also be supplied through the oil bath used to reduce optical lensing effects, although, if kept at too high of a temperature, the index of refraction of the oil bath may change enough to cause lensing. The outer stream could also be heated directly, although controlling the temperature would be challenging due to the high rate of heat loss along the tubing from the ISCO pump to the microfluidic channel. At higher temperatures, nucleation would be expected to occur at higher pressures

(farther upstream in the observation capillary) because temperature drives supersaturation (see reduction in solubility at higher temperatures in Figure II.1). Increasing the temperature alone also increases bubble nucleation by increasing the frequency of “attempts” to nucleate, which is quantified in the scaling of the nucleation energy by  $k_B T$ . At higher temperature, however, the viscosities of the fluids will decrease, increasing the flow speed at a given inlet pressure and leading to greater instability. More viscous polyols may be needed to counteract this effect. Additionally, as discussed in Section VI.5, the nucleation energy barrier can be estimated from the temperature dependence of the nucleation rate using the second nucleation theorem [21, 22].

The effect of temperature ought to be studied before studying the effect of reaction because the reaction of isocyanate with polyol is highly exothermic, so the effects cannot be decoupled. By understanding the effect of higher temperatures on bubble nucleation, the effect of the cross-linking reaction alone would be more easily distinguishable. The effect of this reaction could be studied by flowing isocyanate in the inner stream and observing the reaction along the interface with the polyol in the outer stream (see Figure VII.15b). We hypothesize that the cross-linking reaction and heat will both increase the supersaturation of  $\text{CO}_2$  because  $\text{CO}_2$  is less soluble in polyurethane than polyol and at higher temperatures. The reacting front along the interface between isocyanate and polyol streams is expected to advance into the inner isocyanate stream based on the observations of polyol–isocyanate interfaces by Machuga *et al.* [20]. Based on their work, we might expect the reacting front to advance more than  $50 \mu\text{m}$  within the estimated residence time of about 100 ms, which would consume the entirety of the inner stream. While flowing isocyanate may lead to concerns of fouling, the inner stream will be ensheathed in a much larger volume of polyol, which should react all of the isocyanate before reaching the outlet of the channel. The rate of this reaction  $\tau_{rxn}$  can be varied relative to the depressurization rate  $\tau_{nucl}$  by the addition of catalyst to the polyol in the outer stream. Note that the effect of a cross-linking reaction on foaming could be studied directly by using a photopolymer that cross-links under UV radiation, such as polymers with methacrylate groups.

Upon demonstrating the effects of heat and cross-linking on bubble nucleation, the effect of *in situ*  $\text{CO}_2$  generation could be explored by adding water to the polyol in the outer stream, as shown in Figure VII.15c. This reaction may take seconds to occur, however, so a longer capillary or slower flow rate (through more

viscous polyol or a narrower inner diameter of the observation capillary) may be necessary. This reaction would be accompanied by a cross-linking reaction between polyol and isocyanate and the generation of heat by the exothermic reaction. By performing the other studies first, the effects of these processes on bubble nucleation could be more easily distinguished from those of the CO<sub>2</sub> generation itself.

While not commonly added to polyurethane formulations, microparticles, nanoparticles, and other solid nucleation sites could be added to understand how such particles would affect our results if they turned out to be present in the polyols. Because we did not filter the polyols used in the experiments, there could have been sub-micron particles providing sites for bubble nucleation. Instead of repeating these experiments with filtered polyols, which could be tedious due to the high viscosity of some of these polyols, the presence of particles could be estimated indirectly by *adding* more particles to the system. If adding a certain concentration of particles has a negligible effect on the degree of supersaturation at which bubble nucleation is observed, then we could conclude that the system must already have at least as many particles inside serving as nucleation sites. Talc [23] and fumed silica nanoparticles [24] have been added to enhance bubble nucleation in polymer foams in the literature, but an appropriate nucleant must not degrade the performance of the foam and must be miscible in the mother phase and not agglomerate. Chemical nucleation sites, such as oligomers with several CO<sub>2</sub>-attracting functional groups, could also be used to collect CO<sub>2</sub> molecules and reduce the energy barrier to nucleate a bubble. Amines are generally good at capturing CO<sub>2</sub> and are often used in catalysts for polyurethane foaming [2], which suggests that they may be a compatible source of nucleation sites. Cyclodextrin has also emerged as an effective nucleation site for CO<sub>2</sub>-blown foams due to its cage-like structure's hydrophilic exterior (which promotes miscibility) and hydrophobic interior (which can stabilize clusters of CO<sub>2</sub> molecules) [25]. Cyclodextrin does not agglomerate in the way that silica nanoparticles do, so while increasing the concentration of silica nanoparticles does not increase the amount of bubble nucleation above a certain concentration, the addition of cyclodextrin continues to increase bubble nucleation (see Figure 9 of [25]).

## References

1. Tesser, R., Di Serio, M., Sclafani, A. & Santacesaria, E. Modeling of polyurethane foam formation. *Journal of Applied Polymer Science* **92**, 1875–1886. ISSN: 0021-8995. <https://onlinelibrary.wiley.com/doi/pdf/10.1002/>

- [app.20170](https://onlinelibrary.wiley.com/doi/10.1002/app.20170)<https://onlinelibrary.wiley.com/doi/10.1002/app.20170> (May 2004).
2. *The Polyurethanes Book* (eds Randall, D. & Lee, S.) ISBN: 0470850418 (Huntsman International LLC, Polyurethanes business, 2002).
  3. Brondi, C., Di Maio, E., Bertucelli, L., Parenti, V. & Mosciatti, T. Competing bubble formation mechanisms in rigid polyurethane foaming. *Polymer* **228**, 123877. ISSN: 00323861. <https://doi.org/10.1016/j.polymer.2021.123877><https://linkinghub.elsevier.com/retrieve/pii/S0032386121005000> (July 2021).
  4. Choe, K. H., Lee, D. S., Seo, W. J. & Kim, W. N. Properties of Rigid Polyurethane Foams with Blowing Agents and Catalysts. *Polymer Journal* **36**, 368–373. ISSN: 0032-3896. <http://www.nature.com/doifinder/10.1295/polymj.36.368> (May 2004).
  5. Kang, M. J. *et al.* Liquid nucleating additives for improving thermal insulating properties and mechanical strength of polyisocyanurate foams. *Journal of Materials Science* **45**, 5412–5419. ISSN: 0022-2461. <http://link.springer.com/10.1007/s10853-010-4594-1> (Oct. 2010).
  6. Tompa, H. Phase Relationships in Polymer Solutions. *Trans. Faraday Soc.* **45**, 1142 (1949).
  7. Bungert, B., Sadowski, G. & Arlt, W. Separations and Material Processing in Solutions with Dense Gases. *Ind. Eng. Chem. Res.* **37**, 3208–3220 (1998).
  8. Müller, M., MacDowell, L. G., Virnau, P. & Binder, K. Interface properties and bubble nucleation in compressible mixtures containing polymers. *The Journal of Chemical Physics* **117**, 5480–5496. ISSN: 0021-9606. <http://aip.scitation.org/doi/10.1063/1.1497636> (Sept. 2002).
  9. Talanquer, V. & Oxtoby, D. W. Nucleation of bubbles in binary fluids. *The Journal of Chemical Physics* **102**, 2156–2164. ISSN: 0021-9606. <http://aip.scitation.org/toc/jcp/102/5><http://aip.scitation.org/doi/10.1063/1.468737> (Feb. 1995).
  10. Ostwald, W. Studies on the Formation and Change of Solid Matter. *Z. Phys. Chem.* **22**, 289–302 (1897).
  11. Golini, P. & Guandalini, M. *Polyurethane Rigid Foams* 2013. <https://patents.google.com/patent/WO2013030101A1/en>.
  12. Reignier, J., Alcouffe, P., Méchin, F. & Fenouillot, F. The morphology of rigid polyurethane foam matrix and its evolution with time during foaming – New insight by cryogenic scanning electron microscopy. *Journal of Colloid and Interface Science* **552**, 153–165. ISSN: 00219797. <https://linkinghub.elsevier.com/retrieve/pii/S0021979719305764> (Sept. 2019).

13. Sundar, G. & Widom, B. Three-phase equilibrium in solutions of polystyrene homologues in cyclohexane. *Fluid Phase Equilibria* **40**, 289–303. ISSN: 03783812 (1988).
14. Xiong, Y. & Kiran, E. Prediction of high-pressure phase behaviour in polyethylene/n-pentane/carbon dioxide ternary system with the Sanchez-Lacombe model. *Polymer* **35**, 4408–4415. ISSN: 00323861 (Sept. 1994).
15. Bungert, B., Sadowski, G. & Arlt, W. Supercritical antisolvent fractionation: measurements in the systems monodisperse and bidisperse polystyrene/cyclohexane/carbon dioxide. *Fluid Phase Equilibria* **139**, 349–359. ISSN: 03783812. <https://linkinghub.elsevier.com/retrieve/pii/S0378381297001672> (Dec. 1997).
16. Seckner, A. J., McClellan, A. K. & McHugh, M. A. High-pressure solution behavior of the polystyrene-toluene-ethane system. *AIChE Journal* **34**, 9–16. ISSN: 0001-1541. <http://doi.wiley.com/10.1002/aic.690340103> (Jan. 1988).
17. Eckert, C. J. & Sandler, S. I. Vapor-liquid equilibria for the carbon dioxide-cyclopentane system at 37.7, 45.0, and 60.0 degree.C. *Journal of Chemical & Engineering Data* **31**, 26–28. ISSN: 0021-9568. <https://pubs.acs.org/doi/abs/10.1021/je00043a008> (Jan. 1986).
18. Shah, N. N., Zollweg, J. A. & Streett, W. B. Vapor-Liquid Equilibrium in the System Carbon Dioxide + Cyclopentane from 275 to 493 K at Pressures to 12.2 MPa. *J. Chem. Eng. Data* **36**, 188–192 (1991).
19. Minogue, E. *An in-situ study of the nucleation process of polyurethane rigid foam formation* PhD thesis (Dublin City University, 2000), 1–194. <http://doras.dcu.ie/19076/>.
20. Machuga, S. C., Midje, H. L., Peanasky, J. S., Macosko, C. W. & Ranz, W. E. Microdispersive interfacial mixing in fast polymerizations. *AIChE Journal* **34**, 1057–1064. ISSN: 15475905 (1988).
21. Ford, I. J. Thermodynamic properties of critical clusters from measurements of vapour-liquid homogeneous nucleation rates. *The Journal of Chemical Physics* **105**, 8324–8332. ISSN: 0021-9606. <http://aip.scitation.org/doi/10.1063/1.472687> (Nov. 1996).
22. Laaksonen, A. & Malila, J. in *Nucleation of Water: From Fundamental Science to Atmospheric and Additional Applications* 45–70 (2022).
23. Tammaro, D., Astarita, A., Di Maio, E. & Iannace, S. Polystyrene Foaming at High Pressure Drop Rates. *Industrial and Engineering Chemistry Research* **55**, 5696–5701. ISSN: 15205045 (2016).

24. Pérez-Tamarit, S., Solórzano, E., Mokso, R. & Rodríguez-Pérez, M. In-situ understanding of pore nucleation and growth in polyurethane foams by using real-time synchrotron X-ray tomography. *Polymer* **166**, 50–54. ISSN: 0032-3861. <https://www.sciencedirect.com/science/article/pii/S0032386119300618> (Mar. 2019).
25. Zhou, Y., He, L. & Gong, W. Effect of organic cage nucleating agent structure on nucleating efficiency and the structure-property relationship. *Polymers* **12**, 1–13. ISSN: 20734360 (2020).

## **VII.S1 Further Discussion of Experimental Apparatus**

### **Safety Precautions Taken While Handling Cyclopentane**

Because of the high flammability of cyclopentane and potential to ignite at small weight fractions in atmosphere (about 5 %), extra precautions were taken to keep oxygen sources low. Most importantly, the mixture of polyol and cyclopentane was poured into the Parr reactor and sealed airtight inside a nitrogen glovebox at the Dow TXINN. By keeping the pressure inside the Parr reactor higher than atmospheric pressure, we reduced the likelihood that any oxygen from the atmosphere would enter the Parr reactor during experimentation. As an additional precaution, we set up the experiment inside a walk-in chemical fume hood, which could safely contain a fire or explosion. If these resources are not available, the oxygen content in the Parr reactor can be minimized by running a slow flow of nitrogen gas through the gas-sampling valve of the Parr reactor while sealing the head to purge oxygen from the atmosphere.

### **High-pressure Liquid Injection System (HPLIS)**

The high-pressure liquid injection system (HPLIS) used to vaporize liquid samples for GC analysis is shown in Figure VII.S1. The liquid sample is taken in through the upper port and expelled through a port on the other side to liquid waste, as indicated by the orange arrows. After purging the dead volume in the tubing, a sample can be injected into a stream of the mobile phase of the GC (composed of helium) upon activating a pneumatic piston (air provided at the top of the HPLIS) that injects 500  $\mu\text{L}$  of the upper liquid stream into the lower stream of the mobile phase. At the same time, the piston is heated to 450 °C for 1.25 seconds.

### **VII.S2 Validation of Sampling Method**

First, we calibrated the Agilent gas chromatograph (GC) equipped with two flame ionization detectors (FIDs) inside a Jetanizer (Advanced Research Company) operating at 400 °C, 35 sccm  $\text{H}_2$ , and 350 sccm air. To test the column used for sampling the headspace of the Parr reactor, which would take in a vapor-like sample, we prepared Tedlar bags of 1–10 L in size with various mixtures of  $\text{CO}_2$  and  $\text{N}_2$  as well as mixtures of cyclopentane and  $\text{N}_2$ . The volumes of gas were measured with a custom pump in the Dow TXINN gas chromatography lab. The contents of these Tedlar bags was fed into the GC column by connecting the inlet of the column to the nozzle on the bag and gently squeezing the bag to expel the gas inside. The  $\text{CO}_2$  passed through the column more quickly and could thus be distinguished from the

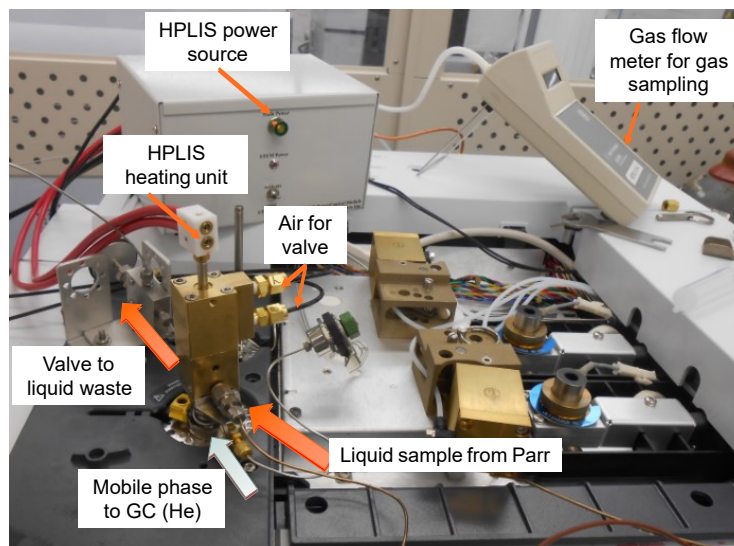


Figure VII.S1: High-pressure liquid injection system (HPLIS) is mounted on gas chromatograph (GC). It receives a liquid sample from the dip tube of the Parr reactor, which enters the HPLIS and exits through a valve to liquid waste normally. A pneumatic valve in the HPLIS pushes the heating unit into the flow of the mobile phase of the GC (helium) and the power source heats the tip to 450 °C to vaporize the cyclopentane and CO<sub>2</sub> so they can enter the GC while leaving behind the polyol.

cyclopentane peak in measurements. In Figure VII.S2, the known density of CO<sub>2</sub> and cyclopentane based on how much was added to the Tedlar bags is plotted on the horizontal axis, and the area under the peak detected by the GC is plotted on the vertical axis. The peak area is indeed proportional to the density for both CO<sub>2</sub> and cyclopentane, and the proportionality constant was used to convert GC peak area measurements into the composition.

To calibrate the GC column for measuring the liquid sample, we sampled CO<sub>2</sub> and cyclopentane differently. Liquid CO<sub>2</sub> was sampled from a dip tube in a liquid CO<sub>2</sub> tank at different split ratios. Cyclopentane samples of different composition were produced by mixing cyclopentane with heptane. In both cases, the liquid sample was passed through the high-pressure liquid injection system (HPLIS), which injected and vaporized a 500 μL sample into the mobile phase of the gas column for measurement.

Next, we used this apparatus to measure the solubility of CO<sub>2</sub> in polyol for comparison to the high-precision measurements of CO<sub>2</sub> solubility made using G-ADSA (see Section II.2). We measured CO<sub>2</sub> solubility at two pressures, 220 psi (1.5 MPa) and 740 psi (5.1 MPa), spanning the low and high end of the G-ADSA measurements. The pressure and measured CO<sub>2</sub> solubility over time are

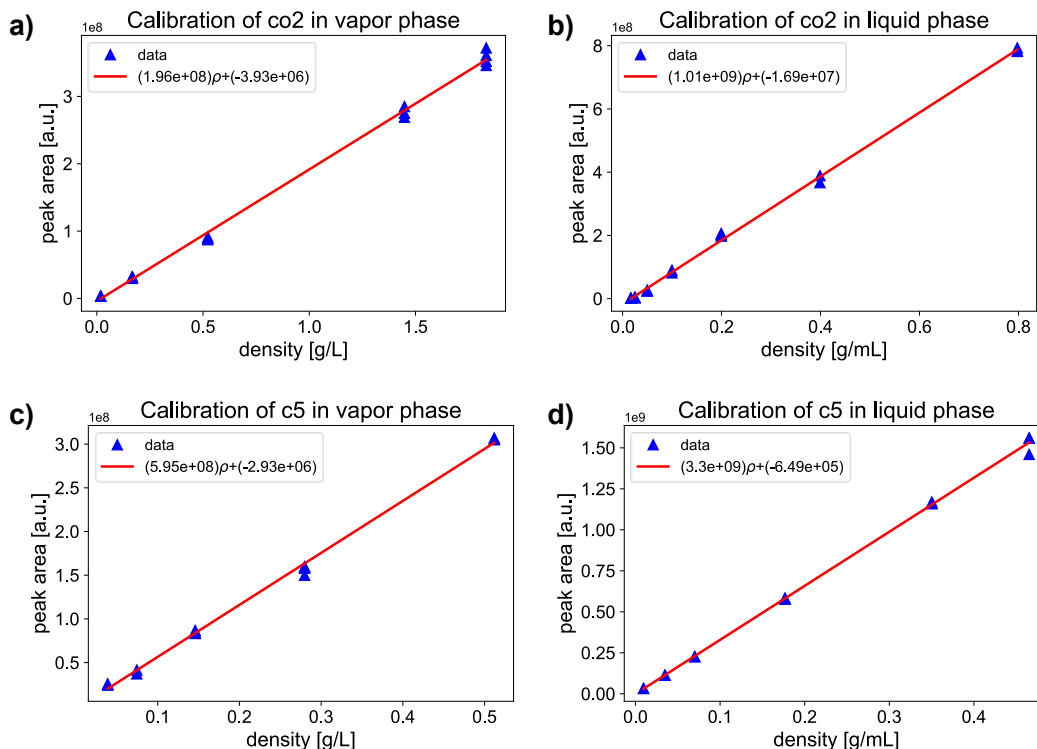


Figure VII.S2: Calibration curves of the gas chromatograph (GC) used to convert integrated peak area into a density. a) CO<sub>2</sub> in vapor phase flame ionization detector (FID). b) CO<sub>2</sub> in liquid phase FID. c) Cyclopentane in vapor phase FID. d) Cyclopentane in liquid phase FID.

shown in Figure VII.S3. The CO<sub>2</sub> solubility measured with GC in this experiment is compared to the measurements made with G-ADSA in Table VII.S1. Because we did not measure the solubility with GC under the exact same conditions as in G-ADSA, we interpolated the solubility values using the PC-SAFT model that successfully fit the measurements (see Figure II.9).

Pressure [MPa]	CO <sub>2</sub> Solub. (GC) [w/w]	CO <sub>2</sub> Solub. (G-ADSA) [w/w]
1.5 ± 0.1	3.9 ± 0.5 %	3.7 + 0.9 % or -0.3 %
5.1 ± 0.1	15 ± 1 %	14.4 + 2.8 % or -2.1 %

Table VII.S1: Estimated CO<sub>2</sub> solubility (weight fraction) at two pressures based on measurements using the high-pressure GC apparatus (Section VII.3) and G-ADSA (Section II.1).

We determined how long we would wait after changing conditions in the Parr reactor by measuring how the measured composition changed over time. Measurements shown in Figure VII.S4.

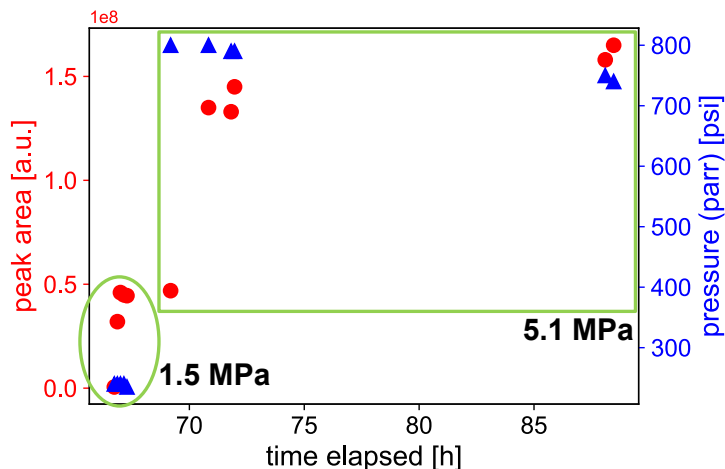


Figure VII.S3: Solubility of CO<sub>2</sub> in 1k2f polyol (see Table II.1) was measured at two pressures, first at 1.5 MPa then, after pressurization, at 5.1 MPa. Integrated area under the peak corresponding to CO<sub>2</sub> is plotted with red circles (left vertical axis), which is proportional to the density (see Figure VII.S2). The pressure inside the Parr reactor is plotted with blue triangles (right vertical axis). The horizontal axis gives the time since the start of the experiment in hours. The points corresponding to the 1.5 MPa pressure measurements are circled while those corresponding to the 5.1 MPa pressure measurements are boxed.

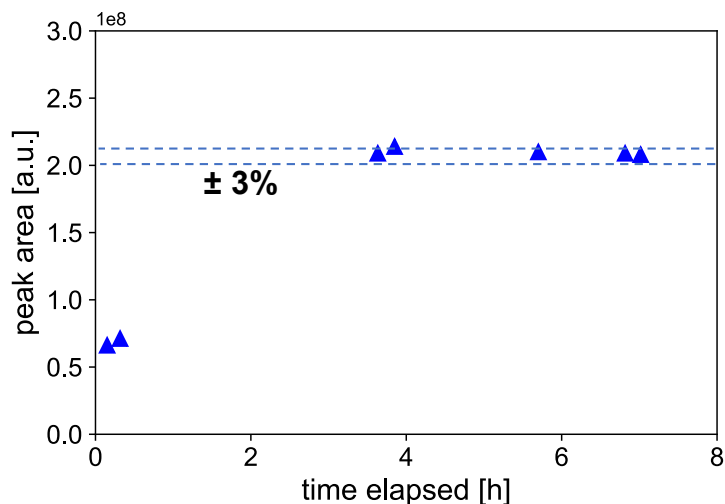


Figure VII.S4: The Parr reactor with about 188 mL (3.5 cm depth) of a 51.5:48.5 mixture of 1k2f polyol (see Table II.1) and cyclopentane is pressurized with CO<sub>2</sub> at time 0. The integrated area under the CO<sub>2</sub> peak measured with GC from samples of the dense liquid phase is plotted as a function of time while the Parr reactor is mixed at 10 RPM. The CO<sub>2</sub> concentration, as measured by the peak area, stabilizes to within 3 % after 4 hours.

### VII.S3 Analysis for Estimating Composition of Each Phase from Sampling Measurements

#### Estimating the Volume of Samples

The volume of fluid sampled is important for many of the estimations of composition in this Section. An important distinction must be made between the volume of sample withdrawn from the Parr reactor and the volume of sample injected into the GC. The volume of sample injected into the GC is fixed by the sampling techniques: the six-port gas-sampling valve holds a sample of about 10  $\mu\text{L}$  of the head space in its tubing for release into the GC and the HPLIS injects and vaporizes a 500  $\mu\text{L}$  sample of the liquid sample into the mobile phase of the GC. The volume of sampled withdrawn from the Parr reactor is typically much larger in order to purge the dead volume between the Parr reactor and the sampling valves. The volume of fluid withdrawn from the head space was measured by a gas flow meter at the outlet. By assuming that the gas equilibrated to atmospheric pressure, we estimated the volume withdrawn  $V_{withdrawn}^V$  by multiplying the estimated density  $\rho_{tot}^V(p_{atm})$  by the volumetric flow rate  $Q^V$  and the time over which the sample was withdrawn  $t^V$  to get  $V_{withdrawn}^V = \rho_{tot}^V(p_{atm})Q^V t^V$ . The volume of fluid withdrawn from the liquid phase was measured by measuring the liquid volume in the waste container (about 2 mL per sample).

#### Estimating the Density of Polyol in the Liquid Sample

Because the HPLIS does not volatilize the polyol and the GC does not detect it, we do not directly measure the density of the polyol in the liquid sample. Instead, we must estimate the density based on the measurements of the cyclopentane and  $\text{CO}_2$  densities and previous knowledge of the equation of state of polyol, cyclopentane,  $\text{CO}_2$ , and mixtures thereof. To perform this estimation, we make two major assumptions. First, we assume that cyclopentane in the liquid phase is incompressible, meaning that we assume that the density of cyclopentane in the liquid phase has the same density at a pressure  $p \in [0.1, 8]$  MPa as at atmospheric pressure (0.1 MPa),  $\rho_{C_5}^L(p) = \rho_{C_5}^L(p_{atm})$ . Second, we assume that the polyol is both incompressible and has the same density as the  $\text{CO}_2$  in the liquid phase, *i.e.*  $\rho_{poly}^L(p) = \rho_{CO_2}^L(p) = \rho_{poly}^L(p_{atm})$ . We base this assumption on our measurements of the specific volume of polyol- $\text{CO}_2$  mixtures under pressure with G-ADSA, which showed that the density changes by less than 5 % (see Figure II.2). While the equality assumed may not be strictly true, we accept the error of 5 % that it incurs.

Because we assume that the polyol is incompressible, the density in the

liquid-phase sample is the density of pure polyol at atmospheric pressure  $\rho_{poly}(p_{atm})$  scaled by the ratio of the volume of polyol  $V_{poly}^{samp}$  in the sample to the total sample volume  $V_{tot}^{samp}$ . The volume of polyol in the sample is

$$V_{poly}^{samp} = V_{tot}^{samp} - V_{CO_2}^{samp} - V_{C_5}^{samp} \quad (\text{VII.4})$$

The volumes of CO<sub>2</sub> and cyclopentane in the sample can be estimated by dividing the density of each measured by GC ( $\rho_{CO_2}^{GC}(p)$  and  $\rho_{C_5}^{GC}(p)$ ) by density of the pure component estimated by the assumptions above. Specifically,  $V_{CO_2}^{samp}/V_{tot}^{samp} \approx \rho_{CO_2}^{GC}(p)/\rho_{poly}(p_{atm})$  and  $V_{C_5}^{samp}/V_{tot}^{samp} \approx \rho_{C_5}^{GC}(p)/\rho_{C_5}^L(p_{atm})$ . Therefore, the estimate for the density of polyol in the liquid sample is

$$\rho_{poly}(p) \approx \rho_{poly}(p_{atm}) \left( 1 - \frac{\rho_{CO_2}^{GC}(p)}{\rho_{poly}(p_{atm})} - \frac{\rho_{C_5}^{GC}(p)}{\rho_{C_5}^L(p_{atm})} \right) \quad (\text{VII.5})$$

where each quantity in equation VII.5 is known from measurement. The weight fractions of each component can then be computed by dividing the density of that component in the sample by the total sample density  $\rho_{samp}(p) = \rho_{poly}(p) + \rho_{C_5}^{GC}(p) + \rho_{CO_2}^{GC}(p)$ .

### Estimating the Vapor Density after Depressurization

Due to the challenges of maintaining pressure inside the sampling apparatus, the sample of vapor from the head space depressurized to atmospheric pressure inside the six-port gas-sampling valve. Consequently, the GC measured a much lower density of CO<sub>2</sub> and cyclopentane in the sample than expected. To correct the effect of depressurization on the densities, we assume that the head space can be treated as a binary mixture of CO<sub>2</sub> and cyclopentane and use a PC-SAFT model fit to such data [1] to estimate the total density  $\rho_{tot}^{pc-saft}$  of the vapor phase under the known pressure and temperature of the Parr reactor. We assume that the weight fractions of CO<sub>2</sub> and cyclopentane remain the same under depressurization. Then we scale the measured densities by the ratio of the PC-SAFT prediction for the total density to the measured total density  $\rho_{tot}^{GC(V)} = \rho_{CO_2}^{GC(V)} + \rho_{C_5}^{GC(V)}$  (where (V) indicates that the measurement is taken of the vapor-phase sample). Then the estimate for the true density of component  $i$  is

$$\rho_i^{true} \approx \left( \frac{\rho_{tot}^{pc-saft}}{\rho_{tot}^{GC(V)}} \right) \rho_i^{GC(V)} \quad (\text{VII.6})$$

### Estimating Density of CO<sub>2</sub> in ISCO Pump

Initially, we believed that the amount of CO<sub>2</sub> in the Parr reactor could be estimated simply by using the CO<sub>2</sub> equation of state to calculate the density and multiply that by the volume dispensed by the ISCO pump into the Parr reactor. This method clearly overestimates the actual amount of CO<sub>2</sub> in the Parr reactor because a substantial amount of CO<sub>2</sub> leaked during the experiment. Additionally, the ISCO pump was likely partially liquid and partially vapor, so determining the overall density of the dispensed fluid was ambiguous. Therefore, we tried two other methods to estimate the amount of CO<sub>2</sub> in the Parr reactor. The first used the change in density of CO<sub>2</sub> in the vapor phase of a CO<sub>2</sub>–C5 binary coexistence at the pressure and temperature before and after adding CO<sub>2</sub>, assuming that CO<sub>2</sub> and C5 had equilibrated immediately after adding CO<sub>2</sub> or C5 to the Parr reactor or venting and that no CO<sub>2</sub> entered the liquid polyol-rich phase. The second used the PC-SAFT model developed by Dr. Huikuan Chao to estimate the composition of the vapor phase. This method is somewhat circular, however, because it relies on the model that the measurements attempt to validate. Nevertheless, it provided a rough estimate of the composition. In both of the latter cases, the estimates suffered from not accounting for the possible presence of a third phase, as depicted in Figure VII.11.

The first method used to estimate the mass of CO<sub>2</sub> in the Parr reactor was estimating how much CO<sub>2</sub> was dispensed from the ISCO pump into the Parr reactor based on the equation of state of CO<sub>2</sub> [2]. The volume and pressure were recorded from the sensor readouts on the ISCO pump both before and after injection of CO<sub>2</sub> into the Parr reactor. The temperature was assumed to remain constant at the lab temperature (about 21 °C). Based on the equation of state of CO<sub>2</sub>, the beginning and final masses of CO<sub>2</sub> in the ISCO pump were estimated, and the difference was taken as an estimate for the amount injected into the Parr reactor.

This method assumed that:

1. The ISCO pump was liquid-full of CO<sub>2</sub> and therefore contained a single, homogeneous phase of CO<sub>2</sub> at all times
2. The Parr reactor did not leak

3. The temperature of the ISCO pump was constant and homogeneous throughout the reservoir
4. The pressure transducer of the ISCO pump did not drift

The first assumption was certainly false after the ISCO pump is refilled because the liquid CO<sub>2</sub> from the tank must expand to fill the dead volume. Additionally, the pressure of the tank is not sufficient to re-condense that vaporized CO<sub>2</sub>. Whether the CO<sub>2</sub> became homogeneously liquid when pressurized to 1000 psi and above before injection was not clear and should be tested with another ISCO pump.

The second assumption was definitely false given the detection of a vapor leak through a needle valve on the gas-sampling port of the Parr reactor. The amount of leaked CO<sub>2</sub> was estimated based on differences in pressure between injections of CO<sub>2</sub> and C5, but these estimates have not been validated by other means.

The third (3) and fourth (4) assumptions are fairly robust, as the steel syringe of the ISCO pump conducts heat well enough to maintain thermal equilibrium with the laboratory and periodic checks of the pressure transducer reading when emptying the ISCO or loading with the liquid CO<sub>2</sub> tank at a known pressure did not show signs of drift beyond 10 psi, which would have a negligible effect on the estimated amount of CO<sub>2</sub> injected in the Parr reactor.

Overall, this first estimation method is likely an *overestimate* of the true mass of CO<sub>2</sub> in the Parr reactor because of the limitations of assumptions (1) and (2) discussed.

The second method of estimating the amount of CO<sub>2</sub> dispensed assumes that, because the amount of polyol in the vapor phase is negligible, the vapor phase can be approximated as the vapor phase of a CO<sub>2</sub>–C5 binary coexistence. Under this assumption, a PC-SAFT model with parameters fitted to Eckert and Sandler's data [1] was used to compute the vapor–liquid equilibrium of CO<sub>2</sub> and C5 at the pressure and temperature in the Parr reactor both before injecting with the ISCO and immediately after. Next, the difference in density of CO<sub>2</sub> in the vapor phase was multiplied by the estimated volume of the vapor phase, which was estimated by subtracting the estimated liquid volume from the approximate interior volume of the Parr reactor (1200 mL). The liquid volume was estimated as  $V_{liq} = m_{poly} / \rho_{poly}^{HPLIS}$ , where  $\rho_{poly}^{HPLIS} = \rho_{poly}^{atm}(T) v_{poly}^{HPLIS}$ , where  $\rho_{poly}^{atm}(T)$  is the estimated density of polyol under atmospheric pressure at the given temperature and  $v_{poly}^{HPLIS}$  is the volumetric

fraction of polyol in the HPLIS, inferred by estimating the volumes of CO<sub>2</sub> and C5 based on their masses measured by the gas chromatograph and their approximate densities at the given temperature.

This method makes the following assumptions:

1. There is no polyol in the vapor phase
2. The vapor-liquid equilibrium between CO<sub>2</sub> and C5 is achieved very rapidly (minutes)
3. The vapor-liquid equilibrium between CO<sub>2</sub> and C5 is not affected by polyol in the liquid phase (*e.g.*, the polyol does not enhance adsorption of CO<sub>2</sub> into the liquid phase)
4. No third phase forms
5. Fitting to Eckert and Sandler's data [1] yields accurate PC-SAFT parameters for the binary coexistence

The first assumption is likely valid because of the low vapor pressure of polyol given its molecular weight of 1000 g/mol and surface tension of almost 30 mN/m. A quick sniff assures the scientist that this is indeed the case.

The second, third, and fourth assumptions have limited validity. The vapor-liquid equilibrium will definitely be affected by the presence of polyol in the liquid as this will lower the diffusivity (hindering equilibrium between vapor-phase and liquid-phase CO<sub>2</sub> and C5) and will affect solubility in the liquid phase. This is made clear when the PC-SAFT estimates of C5 weight fraction in the vapor phase do not match the GC estimates. The fourth assumption is likely false by the sixth injection based on preliminary evidence of the formation of a third phase then, and it is likely that the third phase is present in later measurements as well.

The fifth assumption is probably trustworthy since the data are plentiful and precise.

The advantage of this method is that it only considers changes in CO<sub>2</sub> mass on the order of a few minutes, so we can neglect the leaking of CO<sub>2</sub> and actually use this method as an estimate for how much CO<sub>2</sub> leaked between injections from the ISCO.

## Estimating Mass of Gas Lost through a Leak

We estimated the leak of CO<sub>2</sub> using the CO<sub>2</sub>–C5 binary coexistence method's estimate of the mass of CO<sub>2</sub>. Assuming that changes in the estimated mass are only due to the leaking of CO<sub>2</sub> or injections of CO<sub>2</sub> from the ISCO pump, we took the difference in mass (in general a decrease) between injections from the ISCO and divided by the elapsed time to estimate the rate of leak of CO<sub>2</sub>. We noticed an increase in the rate later in the experiment, around the time that we began to notice leaking through the needle valve on the gas-sampling port of the Parr reactor.

### VII.S4 PC-SAFT Model Details

The parameters of the PC-SAFT model are provided in Table VII.S2. The parameters of cyclopentane were fitted to literature data of the composition of binary mixtures of CO<sub>2</sub> and cyclopentane at different pressures and temperatures [1] while keeping the CO<sub>2</sub> parameters fixed to those values listed in Table II.2. The interaction parameter between cyclopentane and PPG 2700 g/mol was assumed to be the same as between CO<sub>2</sub> and PPG 2700 g/mol listed in Table II.2; this assumption was validated in the main text by the agreement between experimental measurements of the phase composition and the predictions of the PC-SAFT model using these parameters.

Species	$N$ (beads)	$\sigma$ [Å]	$\varepsilon$ [ $k_B$ ]	$k$
C5	2	3.92	290	CO <sub>2</sub> : $-2.9 \times 10^{-6}T + 0.125$ Polyol: $10^{-4}(2T - 590)$

Table VII.S2: The parameters  $N$  (number of beads per chain),  $\sigma$  (bead diameter in Angstroms),  $\varepsilon$  (interaction energy parameter in units of Boltzmann's constant), and  $k$  (cross-interaction parameter between cyclopentane and CO<sub>2</sub> and cyclopentane and PPG 2700 g/mol, unitless, with  $T$  representing the temperature in Kelvin; identical for both species) that fit the solubility data for PPG (2700 g/mol) are listed.

## References

1. Eckert, C. J. & Sandler, S. I. Vapor-liquid equilibria for the carbon dioxide-cyclopentane system at 37.7, 45.0, and 60.0.degree.C. *Journal of Chemical & Engineering Data* **31**, 26–28. ISSN: 0021-9568. <https://pubs.acs.org/doi/abs/10.1021/je00043a008> (Jan. 1986).
2. NIST. *NIST Standard Reference Database Number 69* 2022. <https://webbook.nist.gov/chemistry/> (2022).